Translation of zinc finger domains induces ribosome collision and Znf598-dependent mRNA decay in vertebrates

Kota Ishibashi[1], Yuichi Shichino[2], Peixun Han[2], Kimi Wakabayashi[1], Toshifumi Inada[3], Seisuke Kimura[4,5], Shintaro Iwasaki[2,6], Yuichiro Mishima[1,2‡]

[1] Department of Frontier Life Sciences, Faculty of Life Sciences, Kyoto Sangyo University, Kita-ku, Kyoto 603-8555, Japan
[2] RNA Systems Biochemistry Laboratory, RIKEN Cluster for Pioneering Research, Wako, Saitama 351-0198, Japan
[3] Institute of Medical Science, The University of Tokyo, Minato-Ku, 108-8639, Japan
[4] Department of Industrial Life Sciences, Faculty of Life Sciences, Kyoto Sangyo University, Kita-ku, Kyoto 603-8555, Japan
[5] Center for Plant Sciences, Kyoto Sangyo University, Kita-ku, Kyoto 603-8555, Japan
[6] Department of Computational Biology and Medical Sciences, Graduate School of Frontier Sciences, The University of Tokyo, Kashiwa, Chiba 277-8561, Japan

‡To whom correspondence should be addressed
Email: mishima@cc.kyoto-su.ac.jp

Running title: Zinc finger domains induce ribosome collision and mRNA decay

Abstract

Quality control of translation is crucial for maintaining cellular and organismal homeostasis. Obstacles in translation elongation induce ribosome collision, which is monitored by multiple sensor mechanisms in eukaryotes. The E3 ubiquitin ligase Znf598 recognizes collided ribosomes, triggering ribosome-associated quality control (RQC) to rescue stalled ribosomes and no-go decay (NGD) to degrade stall-prone mRNAs. However, the impact of RQC and NGD on maintaining the translational homeostasis of endogenous mRNAs has remained unclear. In this study, we investigated the endogenous substrate mRNAs of NGD during the maternal-to-zygotic transition (MZT) of zebrafish development. RNA-Seq analysis of zebrafish *znf598* mutant embryos revealed that Znf598 downregulates mRNAs encoding the C2H2-type zinc finger domain (C2H2-ZF) during the MZT. Reporter assays and disome profiling indicated that ribosomes stall and collide while translating tandem C2H2-ZFs, leading to mRNA degradation by Znf598. We further showed that mRNAs encoding C2H2-ZF were degraded in a ZNF598-dependent manner in HEK293T cells. Our results suggest that NGD maintains the quality of the translatome by mitigating the risk of ribosome collision at the abundantly present C2H2-ZF sequences in the vertebrate genome.

(177 words)

Introduction

The translation of mRNA into protein is a fundamental and a costly process in the cell [1]. To minimize the cost of translation and maintain proteome integrity, cells harness multiple quality control mechanisms that prevent faulty translation. The ribosome lies at the core of such translational quality control mechanisms; aberrant positioning, movement, and structure of ribosomes during mRNA translation serve as cues to trigger specific quality control pathways [2,3]. The failure of translational quality control pathways results in the production of harmful proteins and protein aggregates, leading to pathogenic outcomes [4–6].

Persistent stalling of the ribosome during the translation elongation process is detrimental to cells, as it perturbs ribosome traffic on mRNA and exposes the premature polypeptide to the intracellular environment. Ribosomes stall when encountering multiple translational challenges, including tRNA shortages, decoding defects, obstruction by RNA secondary structures, chemical damage to RNA, inhibitory nascent peptide sequences, and combinations thereof [7–9]. Eventually, the trailing ribosome catches up and collides with the leading stalled ribosome, forming an unusual ribosome dimer structure called a disome (or trisome if three ribosomes collide) [10–13]. The cellular machinery recognizes disomes in multiple ways to solve or mitigate translational problems [14,15].

In eukaryotes, the faulty translation leading to disome formation is terminated by splitting the stalled ribosome and degrading the premature nascent polypeptide by ribosome-associated quality control (RQC) [16–18]. In addition, no-go decay (NGD) degrades the mRNA on which ribosomes stall, preventing the accumulation of stall-prone mRNAs [19–21]. Although the coordination and order of RQC and NGD require further investigation, ubiquitination of the stalled ribosome in the disome by ZNF598 (Hel2 in yeast) is the most upstream step in both pathways [12,22–25]. ZNF598/Hel2 ubiquitinates the ribosomal small subunit proteins RPS10/eS10 and RPS20/uS10 at conserved lysine residues, followed by splitting of the stalled ribosome by the RQC-trigger (RQT) complex (also known as the ASC-1 complex; ASCC) [10,24,26–28]. Ubiquitination of the stalled ribosome by ZNF598/Hel2 also induces NGD in yeast and *Caenorhabditis elegans* [11,29,30], partly via the function of the ubiquitin-binding endonuclease Cue2/NONU-1 [30–32]. Alternatively, stall-prone mRNAs might be degraded via GIGYF family proteins that bind to ZNF598/Hel2 [33–35]. Whether vertebrate NGD occurs coincidently with ribosome collision and RQC remains controversial [25,36], but Znf598 is required for stall-induced decay of a reporter mRNA in zebrafish embryos [37]. These observations suggest the presence of a conserved mechanism

acting on RQC and NGD in eukaryotes.

While the molecular mechanism of NGD has been revealed using defined stall-inducing sequences [11,20,30–32,36,38], the endogenous substrate mRNAs of NGD have not been fully characterized. Chemically damaged mRNAs induce ribosome stalling and are potential NGD substrates; however, the frequency of such damage occurring on endogenous mRNAs is unclear [8,39]. Given the widespread distribution of disomes in the transcriptome, it is reasonable to speculate that NGD has a broad impact on endogenous gene expression [40–43]. However, not all disome-forming mRNAs are stabilized in the absence of Hel2 in yeast, making it challenging to identify endogenous mRNAs that are subject to NGD [42]. As a result, only a handful of endogenous NGD target mRNAs have been identified thus far [30,34,36]. Comprehensive identification of the endogenous NGD target mRNAs is needed to understand the physiological role of NGD.

Early embryogenesis is a unique model system for studying mRNA decay *in vivo*. The massive decay of maternal mRNA and concurrent zygotic genome activation (ZGA) constitute a conserved developmental transition in metazoans called the maternal-to-zygotic transition (MZT) [44–47]. The molecular mechanisms underlying MZT have been extensively characterized in zebrafish, in which codon-mediated decay and zygotically transcribed miR-430 play pivotal roles in maternal mRNA clearance in combination with m^6A modification [48–53]. By combining a zebrafish mutant of *znf598* and a reporter mRNA containing a ribosome stall sequence, we previously showed that ribosome stalling induces mRNA decay in a Znf598-dependent manner, demonstrating that NGD is active during the MZT [37]. Codon-mediated decay was unaffected by the loss of Znf598, indicating that NGD is mechanistically distinct from codon-mediated decay [37]. However, the contribution of NGD to shaping the mRNA expression patterns during the MZT has yet to be explored.

In this study, we investigated the endogenous substrate mRNAs of NGD during the MZT using *znf598* mutant zebrafish embryos. Our RNA-Seq analysis showed that Znf598 downregulates mRNAs encoding the C2H2-type zinc finger domain (C2H2-ZF), many of which are expressed zygotically at the onset of MZT. We combined disome profiling and reporter analysis to demonstrate that C2H2-ZF sequences induce ribosome stalling and Znf598-dependent mRNA decay. We further showed that human ZNF598 degrades mRNAs encoding C2H2-ZF. Based on these results, we propose that C2H2-ZF sequences are endogenous ribosome stallers that induce NGD in vertebrates.

Results

The physiological impact of the loss of Znf598 in zebrafish

A zebrafish *znf598* mutant strain with an 11-base deletion in exon 1, predicted to cause frameshifting at the middle of the RING domain, was generated previously [37]. Embryos lacking maternal and zygotic *znf598* activity (MZ*znf598*) are defective in mRNA decay induced by the ribosome stall sequence of hCMV *gp48* uORF2 and cannot ubiquitinate Rps10/eS10 in response to translational stresses [37,54].

To ascertain the physiological impact of the loss of Znf598, we analyzed the viability and growth of the *znf598* mutant strain. Fish obtained by crossing heterozygous *znf598* mutants showed a moderately skewed ratio of genotypes in the tenth week after birth (Supplemental Figure 1A). The difference in the body length between the genotypes was more evident, suggesting that the loss of zygotic *znf598* activity reduced the growth rate (Supplemental Figure 1B). We then crossed *znf598* homozygous males and females to obtain MZ*znf598* embryos. MZ*znf598* embryos were morphologically indistinguishable from wild-type embryos during the gastrulation and prehatching stages (Figure 1A). MZ*znf598* larvae became shorter than wild-type larvae at 5- and 9-days postfertilization (dpf), suggesting the requirement of Znf598 for supporting posthatching larval growth (Figures 1B and C). To further evaluate the growth and survival rates of MZ*znf598,* we cultured the same number of wild-type and MZ*znf598* larvae together in a single tank (Supplemental Figure 1C). Consistent with the analysis of zygotic *znf598* mutant fish, fewer MZ*znf598* fish survived than wild-type fish, and the body length of the survived fish were shorter than those of the wild-type fish at 12 weeks after birth (Supplemental Figure 1D). MZ*znf598* fish eventually caught up with wild-type fish in the body length by 28 weeks after birth without further reduction in survival rate. These results indicate that Znf598 is not obligatory for morphogenesis during embryogenesis but is required for supporting postembryonic growth and survival in zebrafish.

Transcriptome analysis of MZ*znf598* during the MZT

In theory, mRNAs that are degraded via NGD should accumulate in the absence of Znf598. Since NGD reporter mRNA is degraded in a Znf598-dependent manner during the MZT [37], we performed RNA-Seq analysis before (one-hour postfertilization: 1 hpf) and after (6 hpf) the MZT with wild-type and MZ*znf598* embryos to survey endogenous NGD target mRNAs (Figure 2A). Analysis of the RNA-Seq data revealed mRNAs that were significantly

upregulated or downregulated at each stage (FDR<0.01) (Figure 2B). Functional enrichment analysis revealed that no specific term was overrepresented in genes whose expression changed at 1 hpf. In contrast, three specific terms were overrepresented among the genes whose expression changed at 6 hpf (Figure 2C). Notably, two terms related to C2H2-type zinc finger domains (C2H2-ZF) were enriched in genes upregulated at 6 hpf.

To confirm the changes in the mRNA expression of the C2H2-ZF genes in MZ*znf598*, we identified genes encoding C2H2-ZF based on PROSITE annotation and analyzed their expression at 6 hpf. Among the 15245 genes expressed at 6 hpf (>1 count per million mapped reads), 882 genes encoded C2H2-ZF genes. Of those, 57 C2H2-ZF genes were upregulated and 18 genes were downregulated in MZ*znf598* at 6 hpf (FDR<0.01) (Figure 2D). This biased distribution resulted in a significant enrichment of C2H2-ZF genes among the genes upregulated in the MZ*znf598* embryos (57 out of 247 protein-coding genes, 23.1%) compared to all the genes expressed at 6 hpf (882 C2H2-ZF genes out of 15245 protein-coding genes, 5.79%) (Figure 2E and Supplemental Table 1). Consistent with this bias, 61.6% of the C2H2-ZF genes exhibited positive fold changes in expression in MZ*znf598* embryos (543 out of 882 C2H2-ZF genes expressed) (Figure 2F). These trends were not observed with another zinc finger domain, RING-type ZF (RING-ZF) (Figures 2E and F), suggesting a specific impact of Znf598 deficiency on the expression level of C2H2-ZF genes.

To determine the expression patterns of the genes upregulated in MZ*znf598*, we analyzed changes in the mRNA level of these genes during the MZT by comparing RNA-Seq data from wild-type embryos at 1 hpf and 6 hpf. In accordance with the method of the previous study [49], we considered genes whose mRNA level decreased or increased more than twofold from 1 hpf to 6 hpf to be predominantly maternal or zygotic genes, respectively. Other genes were considered maternal-zygotic genes. The numbers of upregulated genes were comparable among the three classes, whereas upregulated C2H2-ZF genes showed a strong bias toward zygotic genes (Figure 2G). These results suggest that the NGD regulates a subset of mRNAs expressed during the MZT and that mRNAs encoding C2H2-ZF are enriched in these mRNAs.

Characterization of maternal NGD target mRNAs

To characterize 74 maternal mRNAs upregulated in MZ*znf598* (maternal NGD target candidates), we compared these mRNAs with previously defined unstable maternal mRNAs degraded during the MZT. In zebrafish, maternal mRNAs with low codon optimality are

degraded via the maternal decay pathway, while mRNAs whose degradation depends on zygotic factors, as exemplified by miR-430, are categorized in the zygotic pathway [48–50]. We found that maternal mRNAs upregulated in MZ*znf598* were distinct from maternal mRNAs degraded by maternal and zygotic decay pathways (Supplemental Figure 2A). Conversely, mRNA degradation via maternal or zygotic decay pathways was unaffected by the loss of Znf598 (Supplemental Figures 2B and C). Similarly, the stability of maternal mRNAs containing m^6A modifications, which act in concert with codon optimality and miR-430 to clear maternal mRNAs [51–53], was unchanged in the MZ*znf598* embryos (Supplemental Figure 2D). These observations support the view that NGD is mechanistically distinct from mRNA decay pathways mediated by codon optimality, miR-430, and m^6A modification.

We selected two C2H2-ZF genes (*znf236* and *znf970*) and three non-C2H2-ZF genes (*ap3s2, mapk14b,* and *piezo2*) from the list of maternal NGD target candidates and validated the RNA-Seq data by qRT–PCR (Figures 3A and B). For this validation, we performed two rescue experiments; MZ*znf598* embryos were injected with mRNAs encoding Myc-tagged full-length Znf598 or a Znf598 mutant lacking the RING domain essential for ribosome ubiquitination and NGD [11,37]. Among the five candidate mRNAs tested, *znf236* and *znf970* were decreased from 2 hpf to 6 hpf in a Znf598- and its RING domain-dependent manner (Figure 3A). Time course qRT–PCR analysis further confirmed that the expression of the *znf236* and *znf970* mRNAs decreased during MZT in wild-type embryos, and this reduction was suppressed in MZ*znf598* embryos (Figure 3C). In contrast, the *ap3s2*, *mapk14b*, and *piezo2* mRNAs accumulated at higher levels in the MZ*znf598* embryos than in the wild-type embryos, as observed in the RNA-Seq data, but were not downregulated by the full-length Znf598 rescue (Figure 3A). These mRNAs might be upregulated indirectly due to the loss of Znf598 in previous stages (e.g., oogenesis). Notably, both *znf236* and *znf970* encoded nearly 30 copies of tandem C2H2-ZFs (Figure 3D).

We further focused on *znf236* mRNA to determine whether its degradation pattern matched the characteristics of NGD. First, we blocked the translation of *znf236* mRNA by injecting a specific morpholino oligonucleotide (MO) that masked the initiation codon from the ribosome [55]. *znf236* mRNA was stabilized in the presence of a specific MO, demonstrating that its degradation required active translation, similar to that of NGD (Figure 3E) [21]. Second, we performed a poly(A) test (PAT) assay for *znf236* mRNA in wild-type

and MZ*znf598* embryos at 6 hpf (Figures 3F and G) [49,56]. *znf236* mRNA was not subject to active deadenylation as observed with the NGD reporter mRNA [37]. These data indicate that maternal C2H2-ZF mRNAs are degraded by a Znf598-dependent mechanism after fertilization.

Characterization of zygotic NGD target mRNAs

Having confirmed the Znf598-dependent decay of maternal C2H2-ZF mRNAs, we next investigated zygotic C2H2-ZF mRNAs upregulated in MZ*znf598* embryos. Many C2H2-ZF genes encode tandem arrays of C2H2-ZFs, with a median of eight C2H2-ZFs per ORF in zebrafish. The number of tandem C2H2-ZF genes often increases via local gene duplication [57], and approximately one-third of C2H2-ZF genes are present on chromosome 4 in zebrafish (401/1115 C2H2-ZF genes in our datasets) [58,59]. A subset of these C2H2-ZF genes shares a characteristic promoter signature with the zygotic miR-430 cluster and are transcribed earlier at the zygotic genome activation (ZGA) during the MZT, followed by transcription of the remaining C2H2-ZF genes [60,61]. Consistent with these studies, mRNAs of C2H2-ZF genes on chromosome 4 were globally upregulated from 1 hpf to 6 hpf according to our wild-type RNA-Seq data (Supplemental Figure 3A). Moreover, C2H2-ZF genes on chromosome 4 were significantly upregulated in MZ*znf598* embryos at 6 hpf, highlighting the pronounced impact of Znf598 on C2H2-ZF genes on chromosome 4 (Figure 4A and Supplemental Figure 3B). We selected three C2H2-ZF genes located on chromosome 4 (*znf1093, si:ch73-266f23.1,* and *znf1102*) from the list of zygotic NGD target candidates and two C2H2-ZF genes on other chromosomes from maternal-zygotic NGD target candidates (*znf1007* and *znf292b*) to validate their Znf598-dependent expression changes by qRT–PCR. All these C2H2-ZF genes were upregulated in MZ*znf598* and suppressed by Znf598 in a RING domain-dependent manner at 6 hpf, indicating the specific downregulation of zygotic C2H2-ZF mRNAs by Znf598 (Figure 4B).

The predominant impact of Znf598 on zygotic C2H2-ZF genes on chromosome 4 prompted us to further investigate the common characteristics of these genes. A recent study identified zygotic C2H2-ZF mRNAs on zebrafish chromosome 4 as cyprinid fish-specific tandem C2H2-ZF genes based on their common gene structure and sequence [62]. The first coding exon of these C2H2-ZF genes typically encodes a fish N-terminal zinc-finger associated (FiNZ) domain, and the second coding exon encodes tandem C2H2-ZFs (Figure 4C). These genes were termed FiNZ-ZNF (FZNF), and 684 genes in the zebrafish genome

were predicted to be FZNF [62] (Figure 4C). Exploiting the sequence similarity of FZNFs, we designed PCR primers that could amplify multiple FiNZ exons in a single PCR reaction (Figure 4C). Genomic qPCR analysis revealed that this primer set amplifies approximately 280 copies of FZNF loci (Figure 4D). This experimental setup allows us to measure the abundance of FZNF mRNAs though qRT–PCR. We observed that FZNF mRNAs were upregulated in MZ*znf598* embryos and suppressed by Znf598 in a RING-domain dependent manner at 6 hpf (Figure 4E).

While the upregulation of FZNF mRNAs in the MZ*znf598* embryos suggested mRNA decay by Znf598, transcriptional activation could also explain the observed changes in expression. To address this possibility, we quantified pre-mRNA levels of FZNF genes using primers that amplify the exon–intron boundary (Figure 4C). We observed that the alterations in pre-mRNA levels were limited compared to those in the mature mRNA levels (Figure 4E). RNA-Seq data further supported this conclusion; reads mapped to intron regions of C2H2-ZF genes showed only marginal upregulation (Supplemental Figure 3C). Even when we subtracted changes in the intron level, we still observed substantial upregulation of the mature mRNA level of C2H2-ZF genes in MZ*znf598* (Supplemental Figure 3D).

Next, we examined whether the FZNF mRNAs were subject to cotranslational mRNA decay. To inhibit the translation of multiple FZNF mRNAs, we utilized a previously reported MO that targeted a highly conserved 5′ UTR sequence upstream of the start codon of more than 200 C2H2-ZF genes on chromosome 4 (znfMO4) [63]. We also designed another MO complementary to the first eight codons of 240 annotated FZNF ORFs (znfMOATG) (Figure 4C). Injection of either MO into wild-type fertilized eggs resulted in specific upregulation of FZNF mRNAs at 6 hpf (Figure 4F). Changes in pre-mRNA levels were limited in the presence of specific MOs, consistent with the expected effect of MOs on translation inhibition. These results demonstrated that Znf598 posttranscriptionally reduces the levels of zygotic FZNF mRNAs during the MZT.

Translation of C2H2-ZF domains causes ribosome stalling and collision

Our RNA-Seq analysis and follow-up experiments suggested that the translation of C2H2-ZF mRNAs caused ribosome stalling and collision, which induced NGD in a Znf598-dependent manner. To validate this model, we examined whether ribosomes indeed stalled while translating the *znf236* ORF using a tandem reporter assay. In this assay, an ORF fragment to be tested was sandwiched between the *Renila* luciferase (Rluc) and firefly

luciferase (Fluc) ORFs, each separated by the P2A ribosome skipping sequence (Figure 5A). Injection of this reporter mRNA into fertilized eggs enables the evaluation of the ribosome elongation rate at the inserted sequence as the ratio of luciferase activities [37]. When we divided the entire ORF of *znf236* into four fragments (fragments 1-4) of comparable length and subjected them to the tandem reporter assay, fragment 1 most strongly inhibited ribosome elongation compared to the other fragments (Figures 5B and C). Further analysis of fragment 1 revealed that two smaller fragments (fragments 1B and 1D) inhibited elongation (Figures 5B and D).

To detect ribosome stalling in the 1B region more directly, we injected an mRNA encoding N-terminally Myc-tagged *znf236* fragment 1 into wild-type and MZ*znf598* fertilized eggs and analyzed the Myc-tagged protein product by Western blotting. While the expression of control Myc-EGFP was unchanged, the expression of the full-length Myc-Znf236 fragment 1 was reduced in the MZ*znf598* embryos (Figure 5E). In addition, we observed an accumulation of smaller products attributable to the peptides that were truncated within the 1B region. These results suggest that ribosomes frequently stall in the 1B region in a nonproductive state and that Znf598 rescues those stalled ribosomes.

Next, we assessed ribosome collision in the 1B region with previously published disome profiling data from the wild type at 4 hpf [40]. Since a subset of C2H2-ZF sequences shares highly homologous sequences at the nucleotide level [58,62], we utilized only uniquely mapped reads containing up to a single mismatch to the reference genome in this study (zebrafish genome assembly GRCz11). As a result, we detected fewer disome peaks in the new analysis than in the previous study (35% fewer peaks in all protein-coding mRNAs and 89% fewer peaks in C2H2-ZF mRNAs) (Supplemental Figure 4A). We then sequenced two additional disome footprint libraries and merged the results with those of the previous two libraries to increase the footprint coverage (see Methods). Although disome footprint reads mapped to the *znf236* ORF was not abundant, 30.5% (18/59) of the reads were clustered in the 1B region (Supplemental Figure 4B, left). These results suggest that ribosomes collide while translating the 1B region of the *znf236* ORF.

The 1B fragment encodes four C2H2-ZFs, and disome footprints were distributed around three C2H2-ZFs: ZF6, ZF7, and ZF8 (Figure 5F). Consistent with the disome profiling results, a fragment encoding three C2H2-ZFs (ZF6-7-8) was sufficient to induce ribosome stalling in the tandem reporter assay (Figure 5G). Ribosome stalling in the C2H2-ZF sequence occurred in a sequence-specific manner because three repeats of ZF6 and ZF8

induced ribosome stalling, whereas ZF7 did not (Figure 5G). At least three copies of ZF6 were required to cause significant ribosome stalling, suggesting the importance of tandem C2H2-ZFs in causing ribosome stalling (Figure 5H).

Having validated ribosome stalling and collision in the C2H2-ZF sequences of *znf236*, we extended our investigation to the C2H2-ZF sequences of zygotic FZNF genes. We selected two FZNF genes validated by qRT–PCR (*znf1102* and *si:ch73-266f23.1*), in which disome footprints were distributed across the ORF at biased densities on C2H2-ZFs (Figure 5I and Supplemental Figure 4B). We then isolated C2H2-ZF sequences with higher disome densities (ZF4-5-6-7 from *znf1102* and ZF3-4-5 from *si:ch73-266f23.1*) and analyzed them via the tandem luciferase reporter assay. These C2H2-ZF sequences induced ribosome stalling at comparable levels to that of *znf236* (Figure 5J). These results indicate that specific tandem C2H2-ZF sequences induce ribosome stalling and collision in zebrafish embryos.

Ribosome collision at C2H2-ZF induces mRNA decay

Following the detection of ribosome collision in model C2H2-ZF sequences, we next investigated the connection between ribosome collision and mRNA degradation. To this end, we performed a reporter mRNA injection assay that detected Znf598-dependent mRNA decay induced by the ribosome stall sequence of hCMV *gp48* uORF2 [37] (Figures 6A and B). We selected 1A-1D fragments of the *znf236* ORF as test cases and inserted them at the 3′ end of the sfGFP ORF. mRNA injection and qRT–PCR revealed that the insertion of fragment 1B destabilized the reporter mRNA in the wild-type embryos but not in the MZ*znf598* embryos (Figure 6B). Furthermore, three repeats of ZF6 (ZF6×3) were sufficient to recapitulate Znf598-dependent mRNA destabilization (Figure 6C). Injection of a MO blocking the translation initiation of the GFP ORF [37,49] into wild-type embryos stabilized the ZF6×3 reporter mRNA to a level comparable to that in MZ*znf598* embryos (Figure 6C), demonstrating that the decay was translation dependent, as it was the case for endogenous *znf236* mRNA (Figure 3E). These results showed that the specific C2H2-ZF sequence of the *znf236* mRNA induces both ribosome stalling and mRNA decay in zebrafish embryos.

To evaluate the connection between ribosome collision and mRNA decay more broadly, we next analyzed the correlation between disome profiling data and RNA-Seq data. We initially focused on disome footprint peaks, as described in a previous study (Supplemental Figure 4A) [40], and detected 65 disome peaks in 37 C2H2-ZF genes expressed at 6 hpf in wild-type embryos. These genes tended to be more upregulated than the

remaining C2H2-ZF genes in the MZ*znf598* embryos (Supplemental Figure 5A). On the other hand, we failed to detect disome peaks in many disome dense regions in the C2H2-ZF sequences (e.g., *znf236*, *znf1102*, and *si:ch73-266f23.1*). This discrepancy occurred because the disome peak analysis aimed to detect strong and consistent ribosome collision at a single codon rather than the high frequency of ribosome collisions in broader regions. Considering these points, we devised a disome localization score, which is the relative accumulation of disome footprints on C2H2-ZF sequences of a given ORF normalized by the total disome footprints formed on the entire ORF (Figure 6D). This domain-wise evaluation gave higher scores if disome footprints were clustered on C2H2-ZF sequences, whereas stochastic or C2H2-ZF-independent disome formation was reflected by lower scores. Based on the disome localization score, we divided the C2H2-ZF mRNAs with disome footprints into three groups (high, middle, and low) (Supplemental Figure 5B). There was no bias in the disome localization score according to the footprint read amount (Supplemental Figure 5C). We found that C2H2-ZF mRNAs in the high group were more upregulated in the MZ*znf598* embryos than those in the middle and low groups (Figure 6E). This genome-wide correlation further supports the model wherein ribosome collision in C2H2-ZF sequences induces mRNA decay in zebrafish embryos.

Sequence features that induce ribosome stalling at C2H2-ZF

To understand the sequence features of C2H2-ZF that cause ribosome collision, we determined the position of the leading ribosome in disome footprints relative to the C2H2-ZF sequence. Approximately 85% of zebrafish C2H2-ZFs are 28 amino acids in length (8168/9622 C2H2-ZFs) and contain cysteine and histidine, which accommodate a zinc ion, at invariant positions (Supplemental Figure 5D) [57,64]. Disomes were formed at various positions in the C2H2-ZF sequence and did not converge at a specific position (Supplemental Figure 5E). Consistent with these results, disome occupancies at the codons on which A-, P-, and E-sites in the leading ribosome lay were not drastically skewed in C2H2-ZF sequences compared to entire ORF sequences (Supplemental Figure 5F). Therefore, ribosomes are unlikely to stall and collide at a consistent position or codon shared in C2H2-ZF sequences.

Electrostatic interactions between the negatively charged ribosome exit tunnel and a positively charged nascent polypeptide are known to cause ribosome stalling and collision [40,41,43,65–67]. Notably, C2H2-ZF proteins presented high isoelectric points (pIs), and C2H2-ZF genes upregulated in the MZ*znf598* embryos encoded proteins with even greater

pIs (Supplemental Figure 5G). Consistent with these data, amino acid sequences encoded upstream of the leading ribosome that stalled at C2H2-ZF had a greater mean net charge than did the control sequences randomly sampled from C2H2-ZF (Supplemental Figure 5H, between 14 and 29 amino acids upstream of the A site). These data indicate that ribosomes stalled in C2H2-ZF sequences tend to hold positively charged peptides in their exit tunnel, possibly contributing to ribosome stalling.

In addition to nascent peptides held in ribosomes, codon sequences also affect the ribosome traversal [68]. Interestingly, genome-wide prediction of mRNA stability by iCodon, which accounts for the effect of codons on mRNA stability, revealed that mRNAs encoding zinc finger transcription factors are significantly unstable in humans [69]. Moreover, iCodon predicted that zebrafish C2H2-ZF genes were significantly unstable, and C2H2-ZF genes upregulated in MZ*znf598* were predicted to be even less stable (Supplemental Figure 5I). Since the effect of codons on mRNA stability is strongly related to the codon decoding rate by the ribosome [37,50,70–72], this prediction indicates that C2H2-ZFs are enriched with codons disadvantageous for translation elongation. Hence, two features that increase the risk of ribosome stalling, positively charged peptides and nonoptimal codons, are inherent in C2H2-ZF sequences.

ZNF598 degrades mRNAs encoding C2H2-ZF proteins in human cells

Finally, we addressed whether the degradation of C2H2-ZF mRNAs by ZNF598 is a conserved phenomenon in vertebrates. To this end, we analyzed mRNA half-lives using BRIC-Seq in HEK293T cells expressing control shRNA or ZNF598-targeting shRNAs (Figure 7A) [40,73]. Among the 3070 transcripts with reliable half-lives, 169 transcripts encoded C2H2-ZF, and 65 encoded RING-ZF. We found that the half-life of transcripts encoding C2H2-ZF was significantly longer in ZNF598 knockdown cells, whereas that of RING-ZF was not (Figure 7B). Like those in zebrafish chromosome 4, many C2H2-ZF mRNAs with increased half-lives in ZNF598 knockdown cells were derived from chromosome 19, where the largest human C2H2-ZF gene cluster is located (Supplemental Figure 6A) [57]. These data indicate that ZNF598 destabilizes mRNAs encoding C2H2-ZF in human cells.

We then compared the BRIC-Seq results with published disome profiling data from HEK293 cells [40]. First, we analyzed whether C2H2-ZF mRNAs with higher disome localization scores were preferentially stabilized in ZNF598 knockdown cells (Supplemental

Figure 6B). Due to the limited number of C2H2-ZF mRNAs analyzed via BRIC-Seq, we divided the C2H2-ZF mRNAs into two groups based on their disome localization scores (top and bottom). Although the small sample size of this analysis hampered the statistical significance of the findings, the half-lives of the top group mRNAs tended to increase more following ZNF598 knockdown than did those of the bottom group mRNAs (Supplemental Figure 6B). When we analyzed the disome position in human C2H2-ZF sequences, disomes formed at C2H2-ZF sequences had no clear positional preference, as observed in zebrafish (Supplemental Figures 6C and D). We also analyzed the mean net charge of nascent polypeptides translated by leading ribosomes stalled at human C2H2-ZF sequences (Supplemental Figure 6E). Nascent polypeptides translated by ribosomes stalled at C2H2-ZF showed a high net charge; however, the high net charge region was more proximal to the decoding/peptidyl transferase centers in humans in zebrafish. These observations imply that a conserved mechanism causes ribosome stalling at C2H2-ZF sequences and mRNA decay by ZNF598 in vertebrates.

Discussion

Toward a comprehensive understanding of ribosome collision and its quality control landscape, we identified mRNAs encoding C2H2-ZF as targets of Znf598-dependent mRNA decay in zebrafish embryos and cultured human cells. Since C2H2-ZF sequences are prone to ribosome stalling and disome formation, our study has revealed that C2H2-ZF sequences are endogenous ribosome stallers that induce NGD in vertebrates (Figure 7C).

Disome profiling in yeast and mammalian cells revealed fundamental sequences of codons and amino acids associated with ribosome collision sites [40–43]. Such stall-prone sequences are often observed between or outside the protein domains [40,43], likely representing programmed ribosome slowdown assisting cotranslational protein folding [74]. In contrast, our understanding of broader protein domains or motifs that are prone to ribosome collision is limited, except for the signal sequences [43,75]. Therefore, it is intriguing that C2H2-ZF, the most abundant DNA-binding domain in the eukaryotic genome [57,76], was identified as a prevalent collision-inducing sequence. The broad distribution of disomes in the C2H2-ZF sequence likely hindered its identification as a typical collision site in previous disome analyses, which have focused mainly on strong and consistent collision sites [40–43]. We speculate that revisiting disome profiling data with the disome density analysis in broader regions will reveal unidentified ribosome stallers. In addition, our study highlighted the importance of combining disome profiling with the analysis of functional consequences, e.g., NGD and RQC, for understanding ribosome collision events that were not characterized by disome profiling alone.

The identification of C2H2-ZF mRNAs as endogenous NGD targets raises questions about the underlying mechanism of ribosome stalling. Since stall-prone C2H2-ZF sequences lack well-established ribosome stalling motifs (e.g., a stretch of lysine AAA codons), they might represent a mechanism distinct from known examples of ribosome collision (Supplemental Figures 5D and 6C) [10,13,36,67,77,78]. As clues to understanding the stalling mechanism, we showed that basic amino acids and nonoptimal codons were enriched in C2H2-ZF sequences prone to NGD (Supplemental Figure 5G-I). A plausible scenario is that the tandem arrangement of the positively charged C2H2-ZF sequence causes sequential exposure of the positively charged nascent polypeptides to the ribosome exit tunnel and synergistically hampers ribosome traverse. The presence of nonoptimal codons in such a sequence context could further increase the risk of ribosome collision. Whether this model explains the general mechanism of ribosome stalling in diverse C2H2-ZF sequences awaits

further validation. Other features, including inhibitory codon and amino acid pairs, cotranslational folding, and interactions with chaperones, might be associated with tandem C2H2-ZF sequences and synergistically contribute to ribosome stalling [79–82]. Elucidation of the detailed ribosome stalling mechanism at the tandem C2H2-ZF sequence will expand our knowledge of ribosome stalling mechanisms in eukaryotes.

Although the stall-prone nature of widespread C2H2-ZF sequences has been revealed, its biological impact has not been fully elucidated. MZ*znf598* embryos develop without apparent morphological defects, suggesting that the failure of RQC or NGD at C2H2-ZF sequences does not perturb the cellular translation status to a catastrophic level (Figure 1 and Supplemental Figure 1). This result is consistent with the normal growth phenotype of the yeast Hel2 mutant [83] and presumably due to the presence of multiple mechanisms that act redundantly to solve or mitigate translation elongation defects, such as GCN1/2, ZAKα, and GTPBP1/2 [84–88]. At the individual transcript level, persistent ribosome collision in the absence of Hel2/ZNF598 could either increase the expression of the full-length protein by allowing readthrough of the stall site or decrease the protein output by roadblocking the following ribosomes [22,24–26,89,90]. Although we observed the latter scenario with a Myc-tagged Znf236 reporter mRNA (Figure 5E), the consequence of the loss of RQC/NGD could be context dependent [14]. mRNA stabilization due to the lack of NGD and loss of the initiation block by the GIGYF-4EHP pathway additionally affect protein output [34,91,92]. As such, the change in the expression of each stall-prone C2H2-ZF protein in the absence of Znf598 is not predictable. In addition, the rapid evolution of C2H2-ZF genes has made it difficult to understand the impact of ribosome collision on protein function. Notably, a recent study proposed the role of FZNF proteins in transposon silencing during MZT [62]. Therefore, perturbation of FZNF expression by the loss of Znf598 might affect transposon silencing and cause genetic alterations on a longer timescale. Alternatively, NGD might contribute to generating the sharp expression peak of FZNFs at ZGA by promoting the clearance of their mRNAs [60,62]. In support of the importance of restricting C2H2-ZF expression, aberrant expression of C2H2-ZF genes has been observed in the zebrafish *kdm2aa* mutant that develops melanoma [93]. Given that ribosome collision in C2H2-ZF is a prevalent and conserved phenomenon, understanding the impact of ribosome collision events in each C2H2-ZF sequence on protein output and phenotypic outcome is an important topic for future studies.

The high propensity of the widely shared C2H2-ZF sequence to stall the ribosome

is a paradoxical phenomenon. The C2H2-ZF domain is the largest protein domain family in the eukaryotic genome, most of which are present as tandem arrays in a protein [57,64]. The evolution of tandem C2H2-ZF genes is highly dynamic, and species-specific amplification of the C2H2-ZF gene is frequently observed [57,58,94]. Accordingly, the repertoire of C2H2-ZF has expanded rapidly, and each species has vast diversity in C2H2-ZF genes [57,95]. On the one hand, the rapid evolution and diversification of the C2H2-ZF sequences are beneficial for expanding the DNA-binding capacity of the proteome to regulate endogenous genes and transposable elements [57,62,95,96]. On the other hand, it could drive the emergence of stall-prone C2H2-ZF sequences at a rate exceeding evolutionary pressure. In this regard, one possible role of NGD is maintaining the quality of the translatome during evolution by reducing the expression of transiently and frequently acquired stall-prone C2H2-ZF sequences.

Finally, our study implies a broad impact of NGD on the expression of both endogenous and artificial repetitive sequences. C2H2-ZF has been engineered as a platform for programmable DNA-binding modules, such as zinc finger nucleases [97]. Elucidation of the ribosome stall mechanism involving the C2H2-ZF sequence would help in the design of efficient DNA-binding modules by preventing stall-prone C2H2-ZF. We also speculate that other tandem repeat domains, which are abundant in the proteome and diversify rapidly [98], harbor a risk of acquiring ribosome stall sequences such as C2H2-ZF. Further studies will elucidate the role of NGD and RQC in the evolution and regulation of mRNAs encoding stall-prone tandem repeats.

Materials and Methods

Zebrafish

The zebrafish AB strain was used as the wild type. The zebrafish *znf598* mutant strain harboring an 11 bp deletion in exon 1 was described previously [37]. Fish were raised and maintained at 28.5°C under standard laboratory conditions according to the Animal Experiment Protocol (2023-37) at Kyoto Sangyo University. Fertilized eggs were obtained by natural breeding. Embryos were developed in system water at 28.5°C. Larvae were fed from 5 dpf after hatching. To compare the viability and growth of wild-type and MZ*znf598* fish, 20 MZ*znf598* embryos were mixed with 20 AB embryos at 1 dpf and raised together in a single tank as described previously [99]. The body length of individual fish was measured and photographed at the indicated times, and the genotype was determined by fin-clipping and genotyping PCR using the primers listed in Supplemental Table 2. Bright-field images were acquired using a SteREO Lumar V12 microscope and an AxioCam MRc camera with ZEN software (Zeiss, Jena, Germany) in spline mode.

Microinjection

Myc-tagged Znf598 mRNAs and tandem ORF luciferase mRNAs were transcribed from a linearized plasmid DNA template using the mMESSAGE mMACHINE SP6 Transcription Kit (Thermo Fisher Scientific) and purified using the RNeasy Mini Kit (QIAGEN). sfGFP, Myc-tagged EGFP, and Myc-tagged Znf236 mRNAs were transcribed from a linearized plasmid DNA template using the SP6-Scribe Standard RNA IVT Kit (CELLSCRIPT), the m^7G cap structure was added to the purified RNA using the ScriptCap m^7G Capping System (CELLSCRIPT), the poly(A) tail was added using the A-Plus Poly(A) Polymerase Tailing Kit (CELLSCRIPT), and the mRNA was purified using the RNeasy Mini Kit. Purified mRNAs were diluted in water to the following concentrations: tandem luciferase mRNAs and sfGFP reporter mRNAs: 50 ng/µl and Myc-Znf598 mRNAs: 200 ng/µl. For injection of Myc-tagged EGFP or Znf236 mRNAs, 50 ng/µl of mRNA and 6 ng/µl QuantiLum Recombinant Luciferase protein (Promega) were coinjected. Microinjection was performed as described previously [37,49] using an IM300 Microinjector (NARISHIGE). Approximately 1,000 pl of the solution was injected per embryo within 15 min of fertilization.

Plasmids

Plasmids for preparing dual-luciferase mRNAs were constructed based on the pLuc plasmid [37]. DNA fragments encoding test sequences were prepared by PCR, annealing complementary oligonucleotides, or DNA fragment synthesis (IDT) and cloned between the EcoRI and XhoI sites of pLuc. The PCR primers used are listed in Supplemental Table 2. To design DNA fragments encoding artificial zinc finger repeats (ZF6×2, 6×3, 7×3, and 8×3), synonymous codon substitutions were introduced to avoid repeat sequences that prohibited DNA fragment synthesis. To construct plasmids for preparing sfGFP mRNAs, DNA fragments encoding test sequences were cloned between the EcoRI and EcoRV sites of the pCS2+neo-sfGFP-*suv39h1a* 3′ UTR [37]. To construct plasmids encoding Myc-tagged EGFP and Znf598 fragment 1, ORFs were amplified via PCR and subsequently inserted into pCS2+MT between the NcoI and EcoRI (EGFP) or EcoRI and XhoI (Znf236 fragment 1) sites. The pCS2+MT-Znf598 plasmids were described previously [37].

RNA-Seq

RNA-Seq was performed as described previously [37]. Briefly, total RNA was extracted from 40–50 wild-type and MZ*znf598* zebrafish embryos at 1 and 6 hpf using TRI Reagent (Molecular Research Center). After DNaseI treatment and purification by the RNeasy Mini Kit, RNA integrity was confirmed using an Agilent RNA 6000 Nano Chip (Agilent Technologies, USA). Total RNA samples were treated with a Ribo-Zero Gold rRNA Removal Kit (Human/Mouse/Rat) (Illumina) and used for RNA-Seq library preparation using an Illumina TruSeq Stranded Total RNA Library Prep Kit (Illumina, USA) with multiplexing. The pooled libraries were sequenced on a NextSeq500 (Illumina) platform with 76 bp single-end sequencing.

Ribosome footprint profiling

A portion of the zebrafish monosome and disome footprint sequencing data at 4 hpf used in this study were published previously [40] (GSE133392). We obtained two additional disome footprint libraries at 4 hpf, corresponding to the mosonome footprint libraries [37] (GSE173604), to increase the depth of disome footprint reads. These additional libraries were prepared in parallel to the published libraries following the protocol described in [100].

Analysis of RNA-Seq data

Zebrafish RNA-Seq data were analyzed using Galaxy on public servers [101]. Single-ended

reads were preprocessed by fastp [102] (version 0.23.2+galaxy0) and mapped to the zebrafish genome reference GRCz11(danRer11) using STAR [103] (version 2.7.8a+galaxy1) by allowing up to a single-nucleotide mismatch with the --outFilterMultimapNmax 1 –outFilterMismatchNmax 1 options. Only uniquely mapped reads were subjected to downstream analysis. Mapped reads were counted by featureCounts [104] (version 2.0.1+galaxy2). To analyze the reads mapped to introns, featureCounts was performed with the GFF feature type filters "transcript" and "exon" with the -O option, and the latter was subtracted from the former. Differential expression was analyzed by edgeR [105] (version 3.36.0+galaxy0). Only genes with Ensemble Canonical transcript annotation were analyzed as protein-coding genes in this study. Genes with at least 1 cpm were considered expressed at detectable levels and were used for further analysis. For the identification of differentially expressed genes, the FDR was set to 0.01. Functional enrichment analysis of the differentially expressed genes was performed using DAVID [106], and mRNAs degraded via maternal and zygotic decay pathways were classified based on a previous study [49]. Maternal mRNAs with high levels of m^6A modification were classified following previous studies [52,53].

Protein domain search and pI analysis

Protein domains in zebrafish and human amino acid sequences were detected using pfsearch [107] (version 2.3.5) based on matrix profiles obtained from the PROSITE database (https://prosite.expasy.org) [108]. The entry IDs of the matrix profiles used are as follows: PS50157 for the C2H2-ZF domain and PS50089 for the RING-ZF domain. The pI of the zebrafish proteins was calculated using the Peptides package in R.

mRNA stability prediction by iCodon

The mRNA stability of the zebrafish genes was predicted from the protein-coding sequences using iCodon algorithm [69]. Only sequences with a length multiple of three were used for the analysis.

Analysis of ribosome profiling data

Ribosome profiling data were processed as previously described [40,109,110] with minor changes. Briefly, reads were preprocessed using fastp [102,103] and mapped to the zebrafish (GRCz11) or human (GRCh38/hg38) reference genome using STAR [103] by allowing up to

a single-nucleotide mismatch and allowing mapping to a single locus with the --outFilterMultimapNmax 1 –outFilterMismatchNmax 1 options. Disome occupancy was calculated as the ratio of reads at given codons to the average reads per codon on all ORFs or on C2H2-ZF domains. The disome localization score was calculated as the ratio of reads on C2H2-ZF domains in an ORF to the total number of reads on the entire ORF. Transcripts with at least 10 reads on the ORF were subjected to downstream analysis. Since most C2H2-ZF domains are 28 amino acids in length, disome occupancies and disome localization scores were calculated for C2H2-ZF domains 28 amino acids in length.

The net charge of a nascent polypeptide associated with the stalled leading ribosome was calculated with 6-amino-acid sliding windows using the Peptides package in R. A-site positions of the leading ribosomes in 28-amino-acid C2H2-ZF domains were used for the net charge calculation (experiment). For the control, the same number of A-site positions in 28-amino-acid C2H2-ZF domains was randomly chosen, and their net charge was calculated (simulation).

BRIC-Seq

Library preparation

BRIC-Seq was performed as described previously with modifications [73]. The HEK293T cells expressing control or ZNF598 shRNA [40] were seeded in 10 cm dishes and incubated in 10 ml of DMEM supplemented with 150 μM bromouridine (BrU, FUJIFILM Wako Pure Chemical Corporation) for 24 h. The cells were then washed twice with 5 ml of DMEM without BrU, incubated in 10 ml of DMEM without BrU for 0, 2, 4, 6, 10, or 24 h, washed with 5 ml of PBS, and lysed by adding 600 μl of TRIzol reagent (Thermo Fisher Scientific) directly to the dishes. Total RNA was purified using a Direct-zol RNA MiniPrep Plus Kit (Zymo Research).

BrU-containing spike-in mRNAs were synthesized via *in vitro* transcription. The template DNA fragments were PCR-amplified using the psiCHECK2 plasmid (Promega) with 5′-TAATACGACTCACTATAGG-3′ and 5′-CACACAAAAAACCAACACACAG-3′ (Rluc); the psiCHECK2 plasmid with 5′-ACTTAATACGACTCACTATAGGAAGCTTGGCATTCCGG-3′ and 5′-TGTATCTTATCATGTCTGCTCGAAG-3′ (Fluc); and the pColdI-GFP plasmid [111] with 5′-TGACTAATACGACTCACTATAGGATCTGTAAAGCACGCCATATCG-3′ and 5′-TGGCAGGGATCTTAGATTCTG-3′ (GFP). *In vitro* transcription was performed using a

T7-Scribe Standard RNA IVT Kit (CELLSCRIPT) in the presence of 1.2 mM BrUTP (Jena Bioscience) and 5 mM UTP. The RNA was purified with RNAClean XP beads (Beckman Coulter).

For immunoprecipitation, 25 µl of Dynabeads M-280 Sheep Anti-Mouse IgG (Thermo Fisher Scientific) was incubated with 2 mg of anti-BrdU antibody (BD Biosciences, 555627) for 3 h at 4°C and equilibrated with BRIC-Seq lysis buffer (lysis buffer without cycloheximide and chloramphenicol). Twenty micrograms of total RNA mixed with a spike-in RNA mixture (1 ng of Rluc, 0.2 ng of Fluc, and 0.04 ng of GFP) was incubated with the magnetic beads in BRIC-Seq lysis buffer for 2 h at 4°C, washed five times with 100 µl of BRIC-Seq lysis buffer, and mixed with 200 µl of TRIzol reagent. RNA was extracted with a Direct-zol RNA MicroPrep Kit and subjected to an RNA-Seq library preparation using a Ribo-Zero Gold rRNA Removal Kit (Human/Mouse/Rat) (Illumina) followed by a TruSeq Stranded Total RNA Kit (Illumina). Libraries were sequenced on a HiSeq 4000 (Illumina) with the single-end/50 nt-long read option.

Data analysis

Filtering by quality and adapter trimming were performed using fastp [102] Reads were subsequently aligned to the noncoding RNAs using STAR 2.7.0a [103] and excluded from analysis. The remaining reads were mapped to the human genome hg38 with the annotation of the GENCODE Human release 32 reference using STAR 2.7.0a with --outFilterMismatchNmax 1 --outFilterMultimapNmax 1 options. The read counts for each transcript were analyzed by featureCounts [104].

The fold changes in read counts compared to those of the 0 h samples were calculated with the DESeq2 package [112] and then renormalized to the mean change in three spike-ins. For the calculation of the mRNA half-life, the $\log_2$-converted fold-change at each time point was fitted to a linear model. Since the decay of transcripts sometimes slows at later time points, we calculated the half-life using all combinations of earlier samples (*i.e.*, 0-4 h, 0-6 h, 0-10 h, and 0-24 h) and fitted the results with the maximum R^2 value. Transcripts with $R^2 > 0.9$ and $0 <$ half-life < 24 h were used in downstream analyses.

<u>qRT–PCR</u>

qRT–PCR analysis of mRNAs was performed as previously described [37]. Briefly, total RNA was prepared using TRI Reagent (Molecular Research Center), and cDNA was

synthesized using the PrimeScript RT reagent kit with gDNA eraser (TaKaRa). A random hexamer was used for cDNA synthesis. qRT–PCR was performed using SYBR Premix Ex TaqII (Tli RNaseH Plus) and the Thermal Cycler Dice Real Time System (TaKaRa). The data were normalized using 18S rRNA as a reference. The sequences of primers used are listed in Supplemental Table 2.

qPCR from genomic DNA

Genomic DNA was extracted from a single wild-type embryo at 24hpf. qPCR analysis of genomic DNA was performed essentially as described for qRT–PCR, except for that genomic DNA was used as a template. Copy numbers of FiNZ exons and *rpl24* were estimated based on a standard curve of a serial dilution of a plasmid containing the amplicon. The copy number of the FiNZ exon was normalized to that of *rpl24* to calculate the copy number per haploid genome. The sequences of primers used are listed in Supplemental Table 2.

PAT assay

The PAT assay was performed as previously described [49]. Briefly, 150 ng of total RNA was incubated with 75 U of yeast poly(A) polymerase (PAP) (Affymetrix) in the presence of GTP/ITP mixure at 37°C for 60 min. cDNA was synthesized at 44°C for 15 min using the PrimeScript RT reagent kit with gDNA eraser (TaKaRa) and the y300 PAT universal C10 primer. PAT-PCR was performed using a 3′ UTR-specific forward primer and a PAT universal primer with GoTaq Green Master Mix (Promega). The PCR products were separated by 6% PAGE in 0.5× TBE. The gels were stained with GelRed (Biotium), and the signals were detected using an Amersham Imager 680 (Cytiva).

Luciferase assay

The luciferase assay was performed as previously described [37]. Briefly, 5–10 embryos were collected at 3 hpf and lysed in Passive Lysis Buffer (Promega) containing cOmplete Protease Inhibitor Cocktail (Sigma–Aldrich). Ten microliters of lysate containing one embryo was used for the assay. The luciferase activities were measured using the Dual-Glo Luciferase Assay System and a GloMax 20/20 luminometer (Promega). The intensity of Fluc activity was normalized to the intensity of Rluc activity. The normalized Fluc activity was further normalized to that of the control sample (no insert).

Western blotting

Proteins were detected as described previously [37] using anti-Myc (MBL Life Science My3 mouse monoclonal, 1:4,000) and anti-α-tubulin-pAb HRP-DirecT (MBL Life Science PM054-7 rabbit polyclonal 1: 10,000) antibodies. To detect Myc-*znf236,* embryos were collected at 6 hpf, and an aliquot of the lysate was subjected to a luciferase assay to ensure the accuracy of the injection amount. Another aliquot of the same lysate was used for Western blotting. The signals were developed using Luminata Forte (Millipore) and detected using an Amersham Imager 680 (Cytiva).

Data availability

The accession numbers for the sequence data reported in this paper are as follows. The GEO datasets used were GSE236143 (RNA-Seq in zebrafish), GSE236144 (additional disome profiling in zebrafish), and GSE233374 (BRIC-Seq).

Acknowledgments

This work was supported by the Japan Society for the Promotion of Science (JSPS) (JP23H02413 and JP22K19300 to YM and JP22K15042 to KI) and the Japan Agency for Medical Research and Development (AMED) (AMED PRIME, JP20gm6310017) to YM. SI was supported by JSPS (JP23H02415), MEXT (JP20H05784), AMED (AMED-CREST, JP20gm1410001), and RIKEN (Pioneering Projects "Biology of Intracellular Environments"). YS was supported by JSPS (JP21K15023 and JP23K05648), MEXT (JP21H05734, 23H04268), and RIKEN (Pioneering Projects "Biology of Intracellular Environments"). SK was supported by JSPS (JP21H02513). PH was supported by the JSPS Research Fellowship for Young Scientists.

We thank our laboratory members for their discussions and critical comments on the project, Kaori Kaminoyama and Tomoaki Sakamoto for RNA-Seq, and Mari Mito for technical assistance. pColdI-GFP was a kind gift from Kotaro Tsuboyama and Yukihide Tomari. DNA libraries for ribosome profiling were sequenced by the Vincent J. Coates Genomics Sequencing Laboratory in QB3 Genomics at UC Berkeley (RRID:SCR_022170) at UC Berkeley (RRID:SCR_022170), supported by the National Institutes for Health (NIH) Instrumentation Grant (S10 OD018174). Computational analysis was supported by the supercomputer HOKUSAI Sailing Ship in RIKEN.

The Galaxy server that was used for some calculations funded in part by the Collaborative Research Centre 992 Medical Epigenetics (DFG grant SFB 992/1 2012) and the German Federal Ministry of Education and Research (BMBF grants 031 A538A/A538C RBC, 031L0101B/031L0101C de.NBI-epi, 031L0106 de.STAIR (de.NBI)).

Author contributions

Y.M. and K.I. designed the project. Y.M., Y.S., and K.W. performed the experiments. K.I., Y.S., P.H., S.I., and Y.M. analyzed the NGS data. S.K. provided the RNA-Seq data. T.I. provided the experimental materials. Y.M. and K.I. drafted the manuscript. All the authors discussed the results and approved the manuscript for submission.

Conflicts of interest

The authors declare that there are no conflicts of interest associated with this manuscript.

Figure legends

Figure 1. Analysis of zebrafish MZ*znf598* embryos and larvae.

(A) Brightfield images of wild-type and MZ*znf598* embryos at the 8-cell stage, shield stage, and 26 hpf. The scale bars indicate 200 µm. (B) Brightfield images of wild-type and MZ*znf598* embryos at 9 dpf. Scale bars indicate 500 µm. (C) Distributions of body length in wild-type and MZ*znf598* fish at 2, 5, and 9 dpf. P values were calculated by the Mann–Whitney U test (two-tailed).

Figure 2. Transcriptome analysis of MZ*znf598* embryos during the MZT.

(A) A scheme of RNA-Seq analysis comparing wild-type and MZ*znf598* embryos during the MZT. (B) Venn diagrams of mRNAs upregulated or downregulated at 1 hpf or 6 hpf (FDR<0.01). The numbers of genes in each category are shown. (C) Functional enrichment analysis of biological terms associated with genes upregulated (pink) or downregulated (light blue) at 6 hpf. Terms that were significantly enriched (FDR<0.01) are shown. (D) A volcano plot showing the fold change in mRNA expression between wild-type and MZ*znf598* embryos at 6 hpf (x-axis) and FDR (y-axis). Genes encoding C2H2-ZF (red) and other genes (gray) are shown. (E) Bar graph showing the fractions of C2H2-ZF or RING-ZF genes among all the genes (gray), genes upregulated in MZ*znf598* (orange), and genes downregulated in MZ*znf598* (blue) at 6 hpf. The p value was calculated by the chi-square test. (F) Cumulative distributions of fold changes in mRNA levels between MZ*znf598* embryos and wild-type embryos at 6 hpf. All genes (black), C2H2-ZF genes (red), and RING-ZF genes (purple) are shown. The x-axis shows the fold change, and the y-axis shows the cumulative fraction. The p values are shown on the right (Kolmogorov–Smirnov test). (G) Bar graphs summarizing the expression patterns of C2H2-ZF genes (red) and other genes (gray) upregulated in MZ*znf598* embryos at 6 hpf.

Figure 3. Validation of maternal mRNAs upregulated in MZ*znf598*.

(A) qRT–PCR analysis of maternal NGD target candidate mRNAs in wild-type (blue) and MZ*znf598* embryos (red) at 6 hpf relative to 2 hpf. The results for MZ*znf598* embryos rescued by injecting mRNAs encoding Myc-tagged full-length Znf598 (light blue) or a mutant Znf598 lacking the RING domain (pink) are also shown. *gstm* mRNA (miR-430 target) and *ddx4* mRNA (stable maternal mRNA) are shown as controls for Znf598-independent maternal mRNAs. (B) Western blotting to detect Myc-tagged Znf598 proteins at 6 hpf.

Tubulin (Tub) was detected as a loading control. (C) Time course qRT–PCR analysis of *znf236* and *znf970* mRNAs in wild-type (blue) and MZ*znf598* (red) embryos. (D) Schematics of the Znf236 and Znf970 proteins. C2H2-ZF is indicated in orange. (E) qRT–PCR analysis of *znf236* mRNA in wild-type and MZ*znf598* embryos at 6 hpf injected with control MO (blue and red) or translation-blocking MO (green and orange). (F) PAT assay of *znf236* mRNA in wild-type and MZ*znf598* embryos at 6 hpf. The lane labeled A0 shows the 3′ UTR fragment without a poly(A) tail. (G) Quantification of the PAT assay in (F). The average values of the two experiments are shown. The graphs represent the average of three independent experiments in A, C, and E. The error bars show the standard deviation. The open circles in A and E show each data point.

Figure 4. Validation of zygotic C2H2-ZF mRNAs upregulated in MZ*znf598*.
(A) Cumulative distributions of fold changes in mRNA levels in MZ*znf598* embryos compared to wild-type embryos at 6 hpf. C2H2-ZF genes on chromosome 4 (orange), C2H2-ZF genes on other chromosomes (purple), and genes without C2H2-ZF (black) are shown. The x-axis shows the fold change, and the y-axis shows the cumulative fraction. The p values are shown on the left (Kolmogorov–Smirnov test). (B) qRT–PCR analysis of C2H2-ZF mRNAs in wild-type (blue) and MZ*znf598* embryos (red) at 6 hpf. The results for MZ*znf598* embryos rescued by injecting mRNAs encoding Myc-tagged full-length Znf598 (light blue) or a mutant Znf598 lacking the RING domain (pink) are also shown. *actb1* mRNA is shown as a control for Znf598-independent mRNA. The chromosomal locations are indicated below the gene name. (C) A scheme of typical FZNF mRNA and corresponding pre-mRNA/genetic loci. (D) Genomic qPCR analysis using primers that amplify exons encoding the FiNZ domain. The estimated copy number of FiNZ exons per haploid genome normalized to that of *rpl24* is shown on the y-axis. (E) qRT–PCR analysis of FZNF mRNAs and pre-mRNAs at 6 hpf. The colors are the same as in (B). (F) qRT–PCR analysis of FZNF mRNAs at 6 hpf in wild-type embryos injected with control MO (blue), znfMO4 (light green), or znfATGMO (green). *znf292b* (a C2H2-ZF gene without the FiNZ domain) and *actb1* (a gene without C2H2-ZF) are shown as controls. The graphs in B, E, and F represent the average of three independent experiments. The graphs in D represent the average of eight independent embryos. The error bars show the standard deviation. The open circles in B, D, E, and F show each data point. Asterisks in E and F indicate $p < 0.05$ (Dunnett's test, compared to wild type or control MO).

Figure 5. Analysis of ribosome stalling sequences in C2H2-ZF mRNAs.
(A) A schematic of the tandem ORF assay. The Rluc ORF (orange) and Fluc ORF (light green) are separated by two P2A translation skipping sequences (blue). The sequence to be tested (shown as X in gray) is inserted between the two P2A sequences. (B) Schematic of the *znf236* ORF fragments analyzed in this study. C2H2-ZF is indicated in orange. Fragments that caused significant ribosome stalling in the tandem luciferase assay are indicated in red. (C and D) Results of the tandem ORF assay with the *znf236* fragment. (E) Western blotting to detect Myc-tagged EGFP (left panel) or Myc-tagged Znf236 fragment 1 in the wild type and MZ*znf598* at 6 hpf. Tubulin (Tub) was detected as a loading control. The predicted positions of Myc-tagged peptides truncated in the Znf236 1A-1D regions are indicated on the right. (F) A detail of the 1B fragment. The amino acid sequences of ZF6, ZF7, and ZF8 are shown below. A-site positions of the stalled leading ribosome and corresponding footprint amounts are indicated as a red gradient. (G) Results of the tandem ORF assay with ZF6, ZF7, or ZF8 repeats. (H) Results of the tandem ORF assay with different numbers of ZF6 repeats. (I) Distributions of disome footprints (blue) in the *znf1102 and si:ch73-266f23.1* ORFs. The amino acid sequences of C2H2-ZFs with high disome footprint amounts are shown below. A-site positions of the stalled leading ribosome and corresponding footprint amounts are indicated as a red gradient. (J) Results of the tandem ORF assay with ZF4-5-6-7 of *znf1102* and ZF3-4-5 of *si:ch73-266f23.1*. The graphs in C, D, G, H and J represent the average of three independent experiments. Relative Fluc signals normalized to Rluc signals are shown. Values with no insert (-) were set to one. The error bars show the standard deviation. The open circles show each data point. Asterisks indicate $p < 0.05$ (Dunnett's test, compared to no insert).

Figure 6. Analysis of the effect of C2H2-ZF sequences on mRNA stability.
(A) A scheme of the mRNA injection assay used to measure the effect of the sequence to be tested (shown as X in gray) on mRNA stability. (B) qRT–PCR analysis of injected sfGFP reporter mRNAs at 6 hpf relative to 2 hpf in wild-type (blue) and MZ*znf598* (red) embryos. (C) qRT–PCR analysis of injected sfGFP-ZF6×3 reporter mRNAs at 6 hpf relative to 2 hpf in wild-type (blue), MZ*znf598* (red), GFP MO-injected wild-type (green), and GFP MO-injected MZ*znf598* (orange) embryos. The graphs in B and C represent the average of three independent experiments. The error bars show the standard deviation. The open circles show

each data point. Asterisks indicate $p < 0.05$ (Student's t-test in B and Dunnett's test compared to the wild type in C). (D) A scheme of the disome localization score analysis. (E) Cumulative distributions of fold changes in mRNA levels in MZ*znf598* embryos compared to wild-type embryos at 6 hpf. All genes (black) and C2H2-ZF genes with high (dark blue), middle (blue), and low (light blue) disome localization scores are shown. The x-axis shows the fold change, and the y-axis shows the cumulative fraction. The p values are shown on the right (Kolmogorov–Smirnov test).

Figure 7. The impact of ZNF598 on the mRNA stability of C2H2-ZF mRNAs in human cells.

(A) A schematic of BRIC-Seq in HEK293T cells. (B) Cumulative distributions of fold changes in the mRNA half-life in HEK293T cells, comparing ZNF598 knockdown cells and control cells. All genes (black), C2H2-ZF genes (red), and RING-ZF genes (purple) are shown. The x-axis shows the fold changes in the mRNA half-life. The p values are shown on the left (Kolmogorov–Smirnov test). (C) A model of NGD for degrading mRNAs encoding stall-prone tandem C2H2-ZF sequences.

Supplemental Figure 1. Additional analysis of the zebrafish *znf598* mutant.

(A) The genotyping results of 10-week-old siblings obtained by crossing heterozygous *znf598* mutant fish. The p value was calculated by the chi-square test. (B) Distributions of body length in 10-week-old wild-type, *znf598* heterozygous, and *znf598* homozygous sibling fish obtained by crossing heterozygous *znf598* mutant fish. The p values were calculated by one-way ANOVA test. (C) A scheme of the growth and survival test comparing wild-type and MZ*znf598* fish. (D) Distributions of the body length in wild-type and MZ*znf598* fish at 12, 16, and 28 weeks after birth. The p values were calculated by the Mann–Whitney U test (two-tailed).

Supplemental Figure 2. Additional information about maternal mRNA analysis in zebrafish embryos.

(A) A Venn diagram of NGD target candidates (yellow), maternal decay mRNAs (pink), and zygotic decay mRNAs (blue). The numbers of genes in each category are shown. (B-D) Cumulative distributions of maternal decay mRNAs, zygotic decay mRNAs, and maternal mRNAs with a high level of m^6A modification. The x-axis shows the fold change in mRNA

expression at 6 hpf compared to 1 hpf in wild-type and MZ*znf598* embryos, and the y-axis shows the cumulative fraction. The p values calculated by the Kolmogorov–Smirnov test are indicated.

Supplemental Figure 3. Additional information about the expression patterns of C2H2-ZF mRNAs in zebrafish.

(A) Chromosomal distributions of C2H2-ZF genes and their relative mRNA expression at 6 hpf compared to 1 hpf in wild-type embryos. The x-axis shows chromosome numbers, and the y-axis shows the fold change in mRNA levels at 6 hpf compared to 1 hpf. (B) Chromosomal distributions of C2H2-ZF genes and their relative mRNA expression in MZ*znf598* embryos compared to wild-type embryos at 6 hpf. The x-axis shows chromosome numbers, and the y-axis shows fold changes in mRNA levels. In A and B, the value of each C2H2-ZF gene is plotted as a dot. The box represents the interquartile range (IQR), with the median indicated by the thick horizontal line in the box. The whiskers represent the variation within 1.5 IQR outside the upper and lower quartiles. (C) Cumulative distributions of fold changes in intron RNA levels in MZ*znf598* embryos compared to wild-type embryos at 6 hpf. (D) Cumulative distributions of the mature mRNA fold change subtracted by the intron RNA fold change in MZ*znf598* embryos compared to wild-type embryos at 6 hpf. In C and D, C2H2-ZF genes on chromosome 4 (orange), C2H2-ZF genes on other chromosomes (purple), and genes without C2H2-ZF (black) are shown. The x-axis shows the fold change, and the y-axis shows the cumulative fraction. The p values are shown on the left (Kolmogorov–Smirnov test).

Supplemental Figure 4. Additional information about disome profiling.

(A) Venn diagrams of disome peaks detected in a previous study [40] and in this study (1 mismatch and unique map). The number of peaks detected in each study is shown. Left: disome peaks in all genes. Right: disome peaks in C2H2-ZF genes. (B) Distributions of monosome (upper, gray) and disome (lower, blue) footprints on the *znf236*, *znf1102*, and *si:ch73-266f23.1* ORFs.

Supplemental Figure 5. Additional information about disome profiling in zebrafish

(A) Cumulative distributions of fold changes in mRNA levels in MZ*znf598* embryos compared to wild-type embryos at 6 hpf. All genes (black) and C2H2-ZF genes with disome

peaks (green) or without disome peaks (light green) are shown. The x-axis shows the fold change, and the y-axis shows the cumulative fraction. The p values are shown on the left (Kolmogorov–Smirnov test). (B) A histogram showing the distributions of disome localization scores on C2H2-ZF genes. The x-axis shows the disome localization score, and the y-axis shows the gene count. (C) A scatter plot showing the disome localization score (x-axis) and total read number for each ORF (y-axis). (D) A logo representation of amino acid diversity among 8168 C2H2-ZF proteins collected from zebrafish genes. (E) A histogram showing the A-site position of the leading ribosome in disome footprints relative to the C2H2-ZF sequence in zebrafish. (F) Disome occupancy at the A-, P-, or E-site codon of the leading stalled ribosome in all genes (x-axis) and C2H2 sequences (y-axis). *rho*, Spearman's rank correlation. (G) Violin plots showing the distribution of the predicted pI values in zebrafish genes. pI values of genes without C2H2-ZF (blue), genes with C2H2-ZF (green), and C2H2-ZF genes upregulated in MZ*znf598* (red) are shown. (H) Mean net charge in the nascent chain around ribosome collision sites on C2H2-ZF sequences in zebrafish. Nascent chain sequences determined by the A-site position of experimentally detected disome footprints (red) and those determined by the randomly chosen A-site position (blue) are shown. (I) Violin plots showing the distribution of the predicted mRNA stability by iCodon in zebrafish genes. The predicted mRNA stabilities of genes without C2H2-ZF (blue), genes with C2H2-ZF (green), and C2H2-ZF genes upregulated in MZ*znf598* (red) are shown. The p values in G and I were calculated by the Wilcoxon rank sum test.

Supplemental Figure 6. Additional information about the mRNA half-life and disome profiling in human cells.

(A) Chromosomal distributions of C2H2-ZF genes and their relative mRNA half-lives in ZNF598 knockdown cells compared to those in control cells. The x-axis shows chromosome numbers, and the y-axis shows the fold change of in the mRNA half-life. The value of each C2H2-ZF gene is plotted as a dot. The box represents the interquartile range (IQR), with the median indicated by the thick horizontal line in the box. The whiskers represent the variation within 1.5 IQR outside the upper and lower quartiles. (B) Cumulative distributions of fold changes in mRNA levels in HEK293T cells, comparing ZNF598 knockdown cells and control cells. All genes (black) and C2H2-ZF genes with top (dark blue) or bottom (light blue) disome localization scores are shown. The x-axis shows the fold change in the mRNA half-life, and the y-axis shows the cumulative fraction. The p values are shown on the left

(Kolmogorov–Smirnov test). (C) A logo representation of amino acid diversity among C2H2-ZF collected from human genes. (D) A histogram showing the A-site position of the leading stalled ribosome in disome footprints relative to the C2H2-ZF sequence in HEK293 cells. (E) Mean net charge in the nascent chains around ribosome collision sites on C2H2-ZF sequences in HEK293 cells. Nascent chain sequences determined by the A-site position of experimentally detected disome footprints (red) and those determined by the randomly chosen A-site position (blue) are shown.

References

1. Hershey JWB, Sonenberg N, Mathews MB. Principles of translational control. Cold Spring Harb Perspect Biol. 2019;11. doi:10.1101/cshperspect.a032607
2. D'Orazio KN, Green R. Ribosome states signal RNA quality control. Mol Cell. 2021. doi:10.1016/j.molcel.2021.02.022
3. Morris C, Cluet D, Ricci EP. Ribosome dynamics and mRNA turnover, a complex relationship under constant cellular scrutiny. Wiley Interdiscip Rev RNA. 2021;12: e1658. doi:10.1002/wrna.1658
4. Stein KC, Morales-Polanco F, van der Lienden J, Rainbolt TK, Frydman J. Ageing exacerbates ribosome pausing to disrupt cotranslational proteostasis. Nature. 2022;601: 637–642. doi:10.1038/s41586-021-04295-4
5. Choe Y-J, Park S-H, Hassemer T, Körner R, Vincenz-Donnelly L, Hayer-Hartl M, et al. Failure of RQC machinery causes protein aggregation and proteotoxic stress. Nature. 2016;531: 191–5. doi:10.1038/nature16973
6. Lu B. Translational regulation by ribosome-associated quality control in neurodegenerative disease, cancer, and viral infection. Front Cell Dev Biol. 2022;10. doi:10.3389/fcell.2022.970654
7. Schuller AP, Green R. Roadblocks and resolutions in eukaryotic translation. Nat Rev Mol Cell Biol. 2018;19: 526–541. doi:10.1038/s41580-018-0011-4
8. Simms CL, Hudson BH, Mosior JW, Rangwala AS, Zaher HS. An Active Role for the Ribosome in Determining the Fate of Oxidized mRNA. Cell Rep. 2014;9: 1256–1264. doi:10.1016/j.celrep.2014.10.042
9. Wilson DN, Arenz S, Beckmann R. Translation regulation via nascent polypeptide-mediated ribosome stalling. Curr Opin Struct Biol. 2016;37: 123–133. doi:10.1016/j.sbi.2016.01.008
10. Matsuo Y, Tesina P, Nakajima S, Mizuno M, Endo A, Buschauer R, et al. RQT complex dissociates ribosomes collided on endogenous RQC substrate SDD1. Nat Struct Mol Biol. 2020;27: 323–332. doi:10.1038/s41594-020-0393-9
11. Ikeuchi K, Tesina P, Matsuo Y, Sugiyama T, Cheng J, Saeki Y, et al. Collided ribosomes form a unique structural interface to induce Hel2-driven quality control pathways. EMBO J. 2019;38: e100276. doi:10.15252/embj.2018100276
12. Juszkiewicz S, Chandrasekaran V, Lin Z, Kraatz S, Ramakrishnan V, Hegde RS. ZNF598 Is a Quality Control Sensor of Collided Ribosomes. Mol Cell. 2018;72: 469-

481.e7. doi:10.1016/j.molcel.2018.08.037

13. Tesina P, Lessen LN, Buschauer R, Cheng J, Wu CC, Berninghausen O, et al. Molecular mechanism of translational stalling by inhibitory codon combinations and poly(A) tracts. EMBO J. 2020;39: 1–17. doi:10.15252/embj.2019103365
14. Meydan S, Guydosh NR. A cellular handbook for collided ribosomes: surveillance pathways and collision types. Curr Genet. 2021;67: 19–26. doi:10.1007/s00294-020-01111-w
15. Kim KQ, Zaher HS. Canary in a coal mine: collided ribosomes as sensors of cellular conditions. Trends Biochem Sci. 2022;47: 82–97. doi:10.1016/j.tibs.2021.09.001
16. Sitron CS, Brandman O. Detection and Degradation of Stalled Nascent Chains via Ribosome-Associated Quality Control. Annu Rev Biochem. 2020;89: 417–442. doi:10.1146/annurev-biochem-013118-110729
17. Filbeck S, Cerullo F, Pfeffer S, Joazeiro CAP. Ribosome-associated quality-control mechanisms from bacteria to humans. Mol Cell. 2022;82: 1451–1466. doi:10.1016/j.molcel.2022.03.038
18. Inada T. Quality controls induced by aberrant translation. Nucleic Acids Res. 2020;48: 1084–1096. doi:10.1093/nar/gkz1201
19. Ikeuchi K, Izawa T, Inada T. Recent Progress on the Molecular Mechanism of Quality Controls Induced by Ribosome Stalling. Front Genet. 2019;9: 1–7. doi:10.3389/fgene.2018.00743
20. Simms CL, Yan LL, Zaher HS. Ribosome Collision Is Critical for Quality Control during No-Go Decay. Mol Cell. 2017;68: 361-373.e5. doi:10.1016/j.molcel.2017.08.019
21. Doma MK, Parker R. Endonucleolytic cleavage of eukaryotic mRNAs with stalls in translation elongation. Nature. 2006;440: 561–4. doi:10.1038/nature04530
22. Sundaramoorthy E, Leonard M, Mak R, Liao J, Fulzele A, Bennett EJ. ZNF598 and RACK1 Regulate Mammalian Ribosome-Associated Quality Control Function by Mediating Regulatory 40S Ribosomal Ubiquitylation. Mol Cell. 2017;65: 751-760.e4. doi:10.1016/j.molcel.2016.12.026
23. Garzia A, Jafarnejad SM, Meyer C, Chapat C, Gogakos T, Morozov P, et al. The E3 ubiquitin ligase and RNA-binding protein ZNF598 orchestrates ribosome quality control of premature polyadenylated mRNAs. Nat Commun. 2017;8: 16056. doi:10.1038/ncomms16056

24. Matsuo Y, Ikeuchi K, Saeki Y, Iwasaki S, Schmidt C, Udagawa T, et al. Ubiquitination of stalled ribosome triggers ribosome-associated quality control. Nat Commun. 2017;8: 159. doi:10.1038/s41467-017-00188-1
25. Juszkiewicz S, Hegde RS. Initiation of Quality Control during Poly(A) Translation Requires Site-Specific Ribosome Ubiquitination. Mol Cell. 2017;65: 743-750.e4. doi:10.1016/j.molcel.2016.11.039
26. Juszkiewicz S, Speldewinde SH, Wan L, Svejstrup JQ, Hegde RS. The ASC-1 Complex Disassembles Collided Ribosomes. Mol Cell. 2020;79: 603-614.e8. doi:10.1016/j.molcel.2020.06.006
27. Hashimoto S, Sugiyama T, Yamazaki R, Nobuta R, Inada T. Identification of a novel trigger complex that facilitates ribosome-associated quality control in mammalian cells. Sci Rep. 2020;10: 3422. doi:10.1038/s41598-020-60241-w
28. Best K, Ikeuchi K, Kater L, Best D, Musial J, Matsuo Y, et al. Structural basis for clearing of ribosome collisions by the RQT complex. Nat Commun. 2023;14: 921. doi:10.1038/s41467-023-36230-8
29. Monem PC, Vidyasagar N, Piatt AL, Sehgal E, Arribere JA. Ubiquitination of stalled ribosomes enables mRNA decay via HBS-1 and NONU-1 in vivo. PLoS Genet. 2023;19: e1010577. doi:10.1371/journal.pgen.1010577
30. Tomomatsu S, Watanabe A, Tesina P, Hashimoto S, Ikeuchi K, Li S, et al. Two modes of Cue2-mediated mRNA cleavage with distinct substrate recognition initiate no-go decay. Nucleic Acids Res. 2023;51: 253–270. doi:10.1093/nar/gkac1172
31. Glover ML, Burroughs AM, Monem PC, Egelhofer TA, Pule MN, Aravind L, et al. NONU-1 Encodes a Conserved Endonuclease Required for mRNA Translation Surveillance. Cell Rep. 2020;30: 4321-4331.e4. doi:10.1016/j.celrep.2020.03.023
32. D'Orazio KN, Wu CC-C, Sinha N, Loll-Krippleber R, Brown GW, Green R. The endonuclease Cue2 cleaves mRNAs at stalled ribosomes during No Go Decay. Elife. 2019;8: 1–27. doi:10.7554/eLife.49117
33. Veltri AJ, D'Orazio KN, Lessen LN, Loll-Krippleber R, Brown GW, Green R. Distinct elongation stalls during translation are linked with distinct pathways for mRNA degradation. Elife. 2022;11. doi:10.7554/eLife.76038
34. Weber R, Chung M-Y, Keskeny C, Zinnall U, Landthaler M, Valkov E, et al. 4EHP and GIGYF1/2 Mediate Translation-Coupled Messenger RNA Decay. Cell Rep. 2020;33: 108262. doi:10.1016/j.celrep.2020.108262

35. Morita M, Ler LW, Fabian MR, Siddiqui N, Mullin M, Henderson VC, et al. A Novel 4EHP-GIGYF2 Translational Repressor Complex Is Essential for Mammalian Development. Mol Cell Biol. 2012;32: 3585–3593. doi:10.1128/mcb.00455-12
36. Arthur LL, Pavlovic-Djuranovic S, Koutmou KS, Green R, Szczesny P, Djuranovic S. Translational control by lysine-encoding A-rich sequences. Sci Adv. 2015;1: e1500154. doi:10.1126/sciadv.1500154
37. Mishima Y, Han P, Ishibashi K, Kimura S, Iwasaki S. Ribosome slowdown triggers codon-mediated mRNA decay independently of ribosome quality control. EMBO J. 2022;41. doi:10.15252/embj.2021109256
38. Chen L, Muhlrad D, Hauryliuk V, Cheng Z, Lim MK, Shyp V, et al. Structure of the Dom34-Hbs1 complex and implications for no-go decay. Nat Struct Mol Biol. 2010;17: 1233–40. doi:10.1038/nsmb.1922
39. Yan LL, Simms CL, McLoughlin F, Vierstra RD, Zaher HS. Oxidation and alkylation stresses activate ribosome-quality control. Nat Commun. 2019;10: 5611. doi:10.1038/s41467-019-13579-3
40. Han P, Shichino Y, Schneider-Poetsch T, Mito M, Hashimoto S, Udagawa T, et al. Genome-wide Survey of Ribosome Collision. Cell Rep. 2020;31: 107610. doi:10.1016/j.celrep.2020.107610
41. Zhao T, Chen YM, Li Y, Wang J, Chen S, Gao N, et al. Disome-seq reveals widespread ribosome collisions that promote cotranslational protein folding. Genome Biol. 2021;22. doi:10.1186/s13059-020-02256-0
42. Meydan S, Guydosh NR. Disome and Trisome Profiling Reveal Genome-wide Targets of Ribosome Quality Control. Mol Cell. 2020; 1–15. doi:10.1016/j.molcel.2020.06.010
43. Arpat AB, Liechti A, De Matos M, Dreos R, Janich P, Gatfield D. Transcriptome-wide sites of collided ribosomes reveal principles of translational pausing. Genome Res. 2020;30: 985–999. doi:10.1101/gr.257741.119
44. Tadros W, Lipshitz HD. The maternal-to-zygotic transition: a play in two acts. Development. 2009;136: 3033–3042. doi:10.1242/dev.033183
45. Despic V, Neugebauer KM. RNA tales - how embryos read and discard messages from mom. J Cell Sci. 2018;131: jcs201996. doi:10.1242/jcs.201996
46. Yartseva V, Giraldez AJ. The Maternal-to-Zygotic Transition During Vertebrate Development: A Model for Reprogramming. Curr Top Dev Biol. 2015;113: 191–232.

doi:10.1016/bs.ctdb.2015.07.020

47. Lee MT, Bonneau AR, Giraldez AJ. Zygotic Genome Activation During the Maternal-to-Zygotic Transition. Annu Rev Cell Dev Biol. 2014;30: 581–613. doi:10.1146/annurev-cellbio-100913-013027
48. Giraldez AJ, Mishima Y, Rihel J, Grocock RJ, Van Dongen S, Inoue K, et al. Zebrafish MiR-430 promotes deadenylation and clearance of maternal mRNAs. Science. 2006;312: 75–9. Available: http://www.ncbi.nlm.nih.gov/pubmed/16484454
49. Mishima Y, Tomari Y. Codon Usage and 3′ UTR Length Determine Maternal mRNA Stability in Zebrafish. Mol Cell. 2016;61: 874–885. doi:10.1016/j.molcel.2016.02.027
50. Bazzini AA, del Viso F, Moreno-Mateos MA, Johnstone TG, Vejnar CE, Qin Y, et al. Codon identity regulates mRNA stability and translation efficiency during the maternal-to-zygotic transition. EMBO J. 2016;35: 2087–2103. doi:10.15252/embj.201694699
51. Medina-Muñoz SG, Kushawah G, Castellano LA, Diez M, DeVore ML, Salazar MJB, et al. Crosstalk between codon optimality and cis-regulatory elements dictates mRNA stability. Genome Biol. 2021;22: 14. doi:10.1186/s13059-020-02251-5
52. Kontur C, Jeong M, Cifuentes D, Giraldez AJ. Ythdf m6A Readers Function Redundantly during Zebrafish Development. Cell Rep. 2020;33: 108598. doi:10.1016/j.celrep.2020.108598
53. Zhao BS, Wang X, Beadell A V., Lu Z, Shi H, Kuuspalu A, et al. m6A-dependent maternal mRNA clearance facilitates zebrafish maternal-to-zygotic transition. Nature. 2017;542: 475–478. doi:10.1038/nature21355
54. Ugajin N, Imami K, Takada H, Ishihama Y, Chiba S, Mishima Y. Znf598-mediated Rps10/eS10 ubiquitination contributes to the ribosome ubiquitination dynamics during zebrafish development. RNA. 2023;29: 1910–1927. doi:10.1261/rna.079633.123
55. Nasevicius A, Ekker SC. Effective targeted gene “knockdown” in zebrafish. Nat Genet. 2000;26: 216–20. doi:10.1038/79951
56. Kusov YY, Shatirishvili G, Dzagurov G, Gauss-Müller V. A new G-tailing method for the determination of the poly(A) tail length applied to hepatitis A virus RNA. Nucleic Acids Res. 2001;29: E57-7. doi:10.1093/nar/29.12.e57
57. Emerson RO, Thomas JH. Adaptive evolution in zinc finger transcription factors. PLoS Genet. 2009;5: e1000325. doi:10.1371/journal.pgen.1000325

58. Howe K, Clark MD, Torroja CF, Torrance J, Berthelot C, Muffato M, et al. The zebrafish reference genome sequence and its relationship to the human genome. Nature. 2013;496: 498–503. doi:10.1038/nature12111
59. Howe K, Schiffer PH, Zielinski J, Wiehe T, Laird GK, Marioni JC, et al. Structure and evolutionary history of a large family of NLR proteins in the zebrafish. Open Biol. 2016;6: 160009. doi:10.1098/rsob.160009
60. White RJ, Collins JE, Sealy IM, Wali N, Dooley CM, Digby Z, et al. A high-resolution mRNA expression time course of embryonic development in zebrafish. Elife. 2017;6. doi:10.7554/eLife.30860
61. Hadzhiev Y, Wheatley L, Cooper L, Ansaloni F, Whalley C, Chen Z, et al. The miR-430 locus with extreme promoter density forms a transcription body during the minor wave of zygotic genome activation. Dev Cell. 2023;58: 155-170.e8. doi:10.1016/j.devcel.2022.12.007
62. Wells JN, Chang N-C, McCormick J, Coleman C, Ramos N, Jin B, et al. Transposable elements drive the evolution of metazoan zinc finger genes. Genome Res. 2023;33: 1325–1339. doi:10.1101/gr.277966.123
63. Hadzhiev Y, Qureshi HK, Wheatley L, Cooper L, Jasiulewicz A, Van Nguyen H, et al. A cell cycle-coordinated Polymerase II transcription compartment encompasses gene expression before global genome activation. Nat Commun. 2019;10: 691. doi:10.1038/s41467-019-08487-5
64. Stubbs L, Sun Y, Caetano-Anolles D. Function and Evolution of C2H2 Zinc Finger Arrays. Subcell Biochem. 2011;52: 75–94. doi:10.1007/978-90-481-9069-0_4
65. Lu J, Deutsch C. Electrostatics in the Ribosomal Tunnel Modulate Chain Elongation Rates. J Mol Biol. 2008;384: 73–86. doi:10.1016/j.jmb.2008.08.089
66. Liutkute M, Samatova E, Rodnina M V. Cotranslational Folding of Proteins on the Ribosome. Biomolecules. 2020;10. doi:10.3390/biom10010097
67. Ito-Harashima S, Kuroha K, Tatematsu T, Inada T. Translation of the poly(A) tail plays crucial roles in nonstop mRNA surveillance via translation repression and protein destabilization by proteasome in yeast. Genes Dev. 2007;21: 519–524. doi:10.1101/gad.1490207
68. Brule CE, Grayhack EJ. Synonymous Codons: Choose Wisely for Expression. Trends in Genetics. Elsevier Ltd; 2017. pp. 283–297. doi:10.1016/j.tig.2017.02.001
69. Diez M, Medina-Muñoz SG, Castellano LA, da Silva Pescador G, Wu Q, Bazzini AA.

iCodon customizes gene expression based on the codon composition. Sci Rep. 2022;12: 12126. doi:10.1038/s41598-022-15526-7

70. Wu Q, Medina SG, Kushawah G, DeVore ML, Castellano LA, Hand JM, et al. Translation affects mRNA stability in a codon-dependent manner in human cells. Elife. 2019;8: 1–22. doi:10.7554/eLife.45396
71. Hanson G, Alhusaini N, Morris N, Sweet T, Coller J. Translation elongation and mRNA stability are coupled through the ribosomal A-site. RNA. 2018;24: 1377–1389. doi:10.1261/rna.066787.118
72. Presnyak V, Alhusaini N, Chen YH, Martin S, Morris N, Kline N, et al. Codon optimality is a major determinant of mRNA stability. Cell. 2015;160: 1111–1124. doi:10.1016/j.cell.2015.02.029
73. Tani H, Mizutani R, Salam KA, Tano K, Ijiri K, Wakamatsu A, et al. Genome-wide determination of RNA stability reveals hundreds of short-lived noncoding transcripts in mammals. Genome Res. 2012;22: 947–956. doi:10.1101/gr.130559.111
74. Kramer G, Shiber A, Bukau B. Mechanisms of Cotranslational Maturation of Newly Synthesized Proteins. Annu Rev Biochem. 2019;88: 337–364. doi:10.1146/annurev-biochem-013118-111717
75. Matsuo Y, Inada T. The ribosome collision sensor Hel2 functions as preventive quality control in the secretory pathway. Cell Rep. 2021;34: 108877. doi:10.1016/j.celrep.2021.108877
76. Schmitz JF, Zimmer F, Bornberg-Bauer E. Mechanisms of transcription factor evolution in Metazoa. Nucleic Acids Res. 2016;44: 6287–97. doi:10.1093/nar/gkw492
77. Guydosh NR, Green R. Translation of poly(A) tails leads to precise mRNA cleavage. RNA. 2017;23: 749–761. doi:10.1261/rna.060418.116
78. Chandrasekaran V, Juszkiewicz S, Choi J, Puglisi JD, Brown A, Shao S, et al. Mechanism of ribosome stalling during translation of a poly(A) tail. Nat Struct Mol Biol. 2019;26: 1132–1140. doi:10.1038/s41594-019-0331-x
79. Nilsson OB, Hedman R, Marino J, Wickles S, Bischoff L, Johansson M, et al. Cotranslational Protein Folding inside the Ribosome Exit Tunnel. Cell Rep. 2015;12: 1533–40. doi:10.1016/j.celrep.2015.07.065
80. Stein KC, Kriel A, Frydman J. Nascent Polypeptide Domain Topology and Elongation Rate Direct the Cotranslational Hierarchy of Hsp70 and TRiC/CCT. Mol Cell. 2019;75: 1117-1130.e5. doi:10.1016/j.molcel.2019.06.036

81. Gamble CE, Brule CE, Dean KM, Fields S, Grayhack EJ. Adjacent Codons Act in Concert to Modulate Translation Efficiency in Yeast. Cell. 2016;166: 679–690. doi:10.1016/j.cell.2016.05.070
82. Burke PC, Park H, Subramaniam AR. A nascent peptide code for translational control of mRNA stability in human cells. Nat Commun. 2022;13: 6829. doi:10.1038/s41467-022-34664-0
83. Singh RK, Gonzalez M, Kabbaj M-HM, Gunjan A. Novel E3 ubiquitin ligases that regulate histone protein levels in the budding yeast Saccharomyces cerevisiae. PLoS One. 2012;7: e36295. doi:10.1371/journal.pone.0036295
84. Wu CC, Peterson A, Zinshteyn B, Regot S, Green R. Ribosome Collisions Trigger General Stress Responses to Regulate Cell Fate. Cell. 2020;182: 404-416.e14. doi:10.1016/j.cell.2020.06.006
85. Vind AC, Snieckute G, Blasius M, Tiedje C, Krogh N, Bekker-Jensen DB, et al. ZAKα Recognizes Stalled Ribosomes through Partially Redundant Sensor Domains. Mol Cell. 2020;78: 700-713.e7. doi:10.1016/j.molcel.2020.03.021
86. Pochopien AA, Beckert B, Kasvandik S, Berninghausen O, Beckmann R, Tenson T, et al. Structure of Gcn1 bound to stalled and colliding 80S ribosomes. Proceedings of the National Academy of Sciences. 2021;118: e2022756118. doi:10.1073/pnas.2022756118
87. Terrey M, Adamson SI, Gibson AL, Deng T, Ishimura R, Chuang JH, et al. GTPBP1 resolves paused ribosomes to maintain neuronal homeostasis. Elife. 2020;9: 1–22. doi:10.7554/eLife.62731
88. Ishimura R, Nagy G, Dotu I, Zhou H, Yang X-L, Schimmel P, et al. Ribosome stalling induced by mutation of a CNS-specific tRNA causes neurodegeneration. Science (1979). 2014;345: 455–459. doi:10.1126/science.1249749
89. Letzring DP, Wolf AS, Brule CE, Grayhack EJ. Translation of CGA codon repeats in yeast involves quality control components and ribosomal protein L1. RNA. 2013;19: 1208–17. doi:10.1261/rna.039446.113
90. Brandman O, Stewart-Ornstein J, Wong D, Larson A, Williams CC, Li G-W, et al. A ribosome-bound quality control complex triggers degradation of nascent peptides and signals translation stress. Cell. 2012;151: 1042–54. doi:10.1016/j.cell.2012.10.044
91. Hickey KL, Dickson K, Cogan JZ, Replogle JM, Schoof M, D'Orazio KN, et al. GIGYF2 and 4EHP Inhibit Translation Initiation of Defective Messenger RNAs to

Assist Ribosome-Associated Quality Control. Mol Cell. 2020;79: 950-962.e6. doi:10.1016/j.molcel.2020.07.007

92. Juszkiewicz S, Slodkowicz G, Lin Z, Freire-Pritchett P, Peak-Chew S-Y, Hegde RS. Ribosome collisions trigger cis-acting feedback inhibition of translation initiation. Elife. 2020;9: 1–29. doi:10.7554/eLife.60038

93. Scahill CM, Digby Z, Sealy IM, Wojciechowska S, White RJ, Collins JE, et al. Loss of the chromatin modifier Kdm2aa causes BrafV600E-independent spontaneous melanoma in zebrafish. PLoS Genet. 2017;13: e1006959. doi:10.1371/journal.pgen.1006959

94. Kauzlaric A, Ecco G, Cassano M, Duc J, Imbeault M, Trono D. The mouse genome displays highly dynamic populations of KRAB-zinc finger protein genes and related genetic units. PLoS One. 2017;12: e0173746. doi:10.1371/journal.pone.0173746

95. Imbeault M, Helleboid P-Y, Trono D. KRAB zinc-finger proteins contribute to the evolution of gene regulatory networks. Nature. 2017;543: 550–554. doi:10.1038/nature21683

96. Schmitges FW, Radovani E, Najafabadi HS, Barazandeh M, Campitelli LF, Yin Y, et al. Multiparameter functional diversity of human C2H2 zinc finger proteins. Genome Res. 2016;26: 1742–1752. doi:10.1101/gr.209643.116

97. Klug A. The discovery of zinc fingers and their applications in gene regulation and genome manipulation. Annu Rev Biochem. 2010;79: 213–31. doi:10.1146/annurev-biochem-010909-095056

98. Kajava A V. Tandem repeats in proteins: from sequence to structure. J Struct Biol. 2012;179: 279–88. doi:10.1016/j.jsb.2011.08.009

99. Zhao X, Ma D, Ishiguro K, Saito H, Akichika S, Matsuzawa I, et al. Glycosylated queuosines in tRNAs optimize translational rate and post-embryonic growth. Cell. 2023;186: 5517-5535.e24. doi:10.1016/j.cell.2023.10.026

100. Mito M, Mishima Y, Iwasaki S. Protocol for Disome Profiling to Survey Ribosome Collision in Humans and Zebrafish. STAR Protoc. 2020;1: 100168. doi:10.1016/j.xpro.2020.100168

101. Galaxy Community. The Galaxy platform for accessible, reproducible and collaborative biomedical analyses: 2022 update. Nucleic Acids Res. 2022;50: W345–W351. doi:10.1093/nar/gkac247

102. Chen S, Zhou Y, Chen Y, Gu J. fastp: an ultra-fast all-in-one FASTQ preprocessor.

Bioinformatics. 2018;34: i884–i890. doi:10.1093/bioinformatics/bty560

103. Dobin A, Davis CA, Schlesinger F, Drenkow J, Zaleski C, Jha S, et al. STAR: ultrafast universal RNA-seq aligner. Bioinformatics. 2013;29: 15–21. doi:10.1093/bioinformatics/bts635
104. Liao Y, Smyth GK, Shi W. featureCounts: an efficient general purpose program for assigning sequence reads to genomic features. Bioinformatics. 2014;30: 923–30. doi:10.1093/bioinformatics/btt656
105. Robinson MD, McCarthy DJ, Smyth GK. edgeR: a Bioconductor package for differential expression analysis of digital gene expression data. Bioinformatics. 2010;26: 139–40. doi:10.1093/bioinformatics/btp616
106. Sherman BT, Hao M, Qiu J, Jiao X, Baseler MW, Lane HC, et al. DAVID: a web server for functional enrichment analysis and functional annotation of gene lists (2021 update). Nucleic Acids Res. 2022;50: W216–W221. doi:10.1093/nar/gkac194
107. Bucher P, Karplus K, Moeri N, Hofmann K. A flexible motif search technique based on generalized profiles. Comput Chem. 1996;20: 3–23. doi:10.1016/s0097-8485(96)80003-9
108. Sigrist CJA, de Castro E, Cerutti L, Cuche BA, Hulo N, Bridge A, et al. New and continuing developments at PROSITE. Nucleic Acids Res. 2013;41: D344-7. doi:10.1093/nar/gks1067
109. Iwasaki S, Floor SN, Ingolia NT. Rocaglates convert DEAD-box protein eIF4A into a sequence-selective translational repressor. Nature. 2016;534: 558–61. doi:10.1038/nature17978
110. Ingolia NT, Brar GA, Rouskin S, McGeachy AM, Weissman JS. The ribosome profiling strategy for monitoring translation in vivo by deep sequencing of ribosome-protected mRNA fragments. Nat Protoc. 2012;7: 1534–50. doi:10.1038/nprot.2012.086
111. Tsuboyama K, Osaki T, Matsuura-Suzuki E, Kozuka-Hata H, Okada Y, Oyama M, et al. A widespread family of heat-resistant obscure (Hero) proteins protect against protein instability and aggregation. PLoS Biol. 2020;18: e3000632. doi:10.1371/journal.pbio.3000632
112. Love MI, Huber W, Anders S. Moderated estimation of fold change and dispersion for RNA-seq data with DESeq2. Genome Biol. 2014;15: 550. doi:10.1186/s13059-014-0550-8

Ishibashi et al., Figure 1

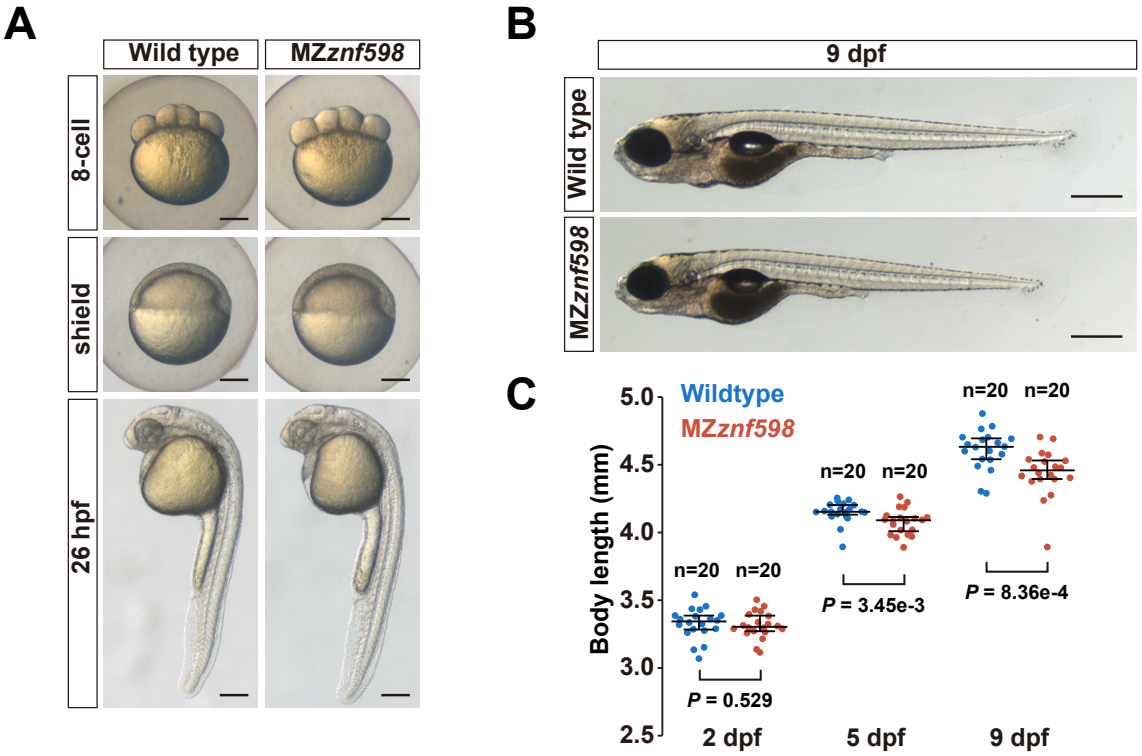

Ishibashi et al., Figure 2

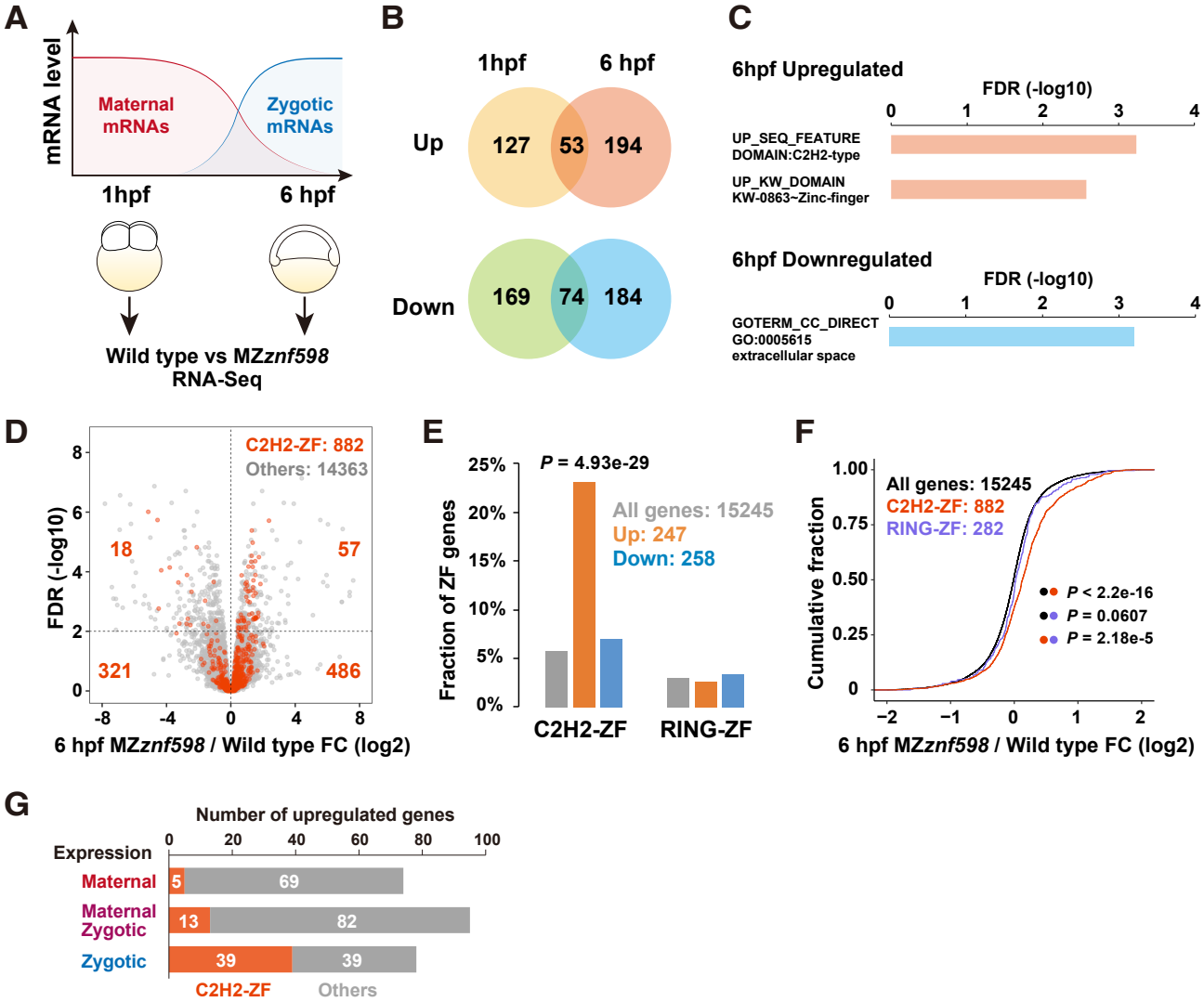

Ishibashi et al., Figure 3

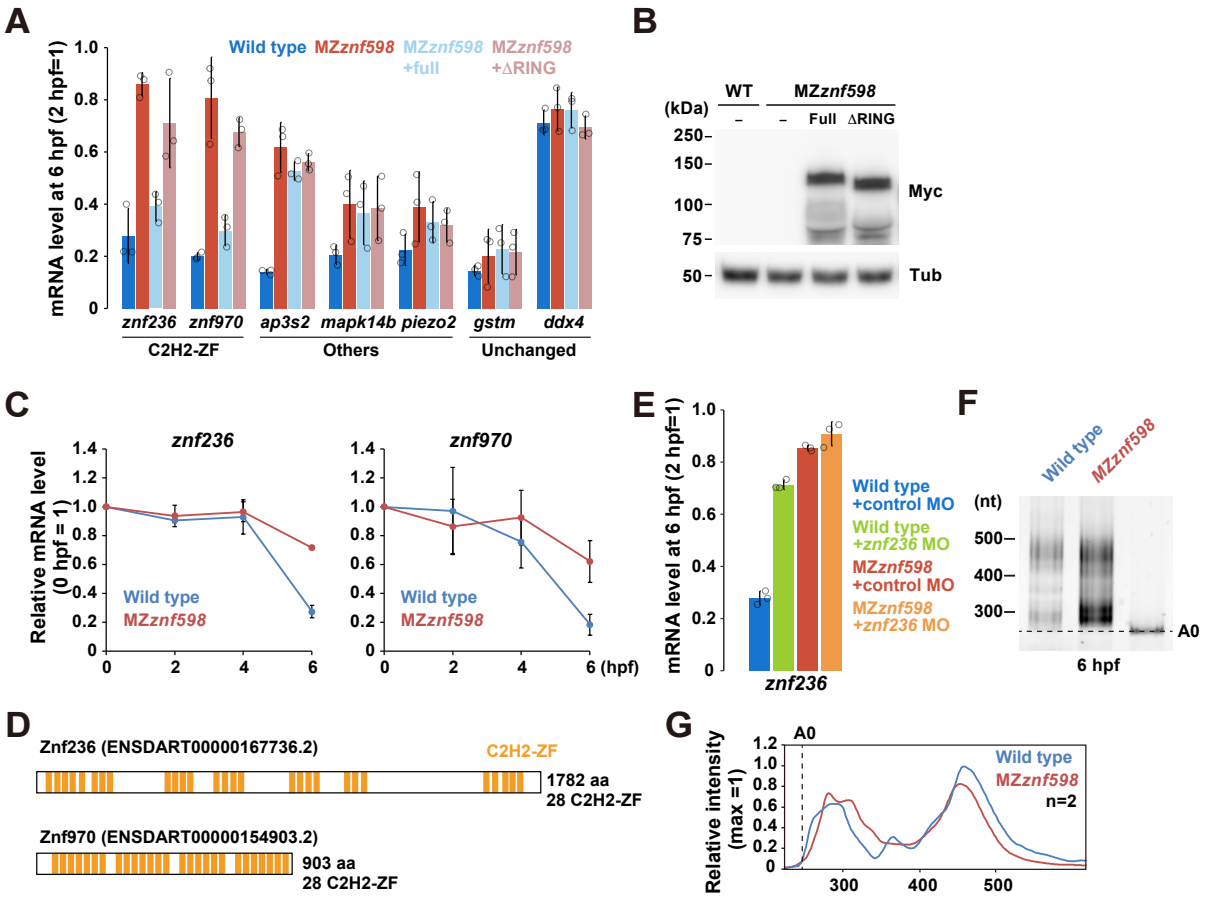

Ishibashi et al., Figure 4

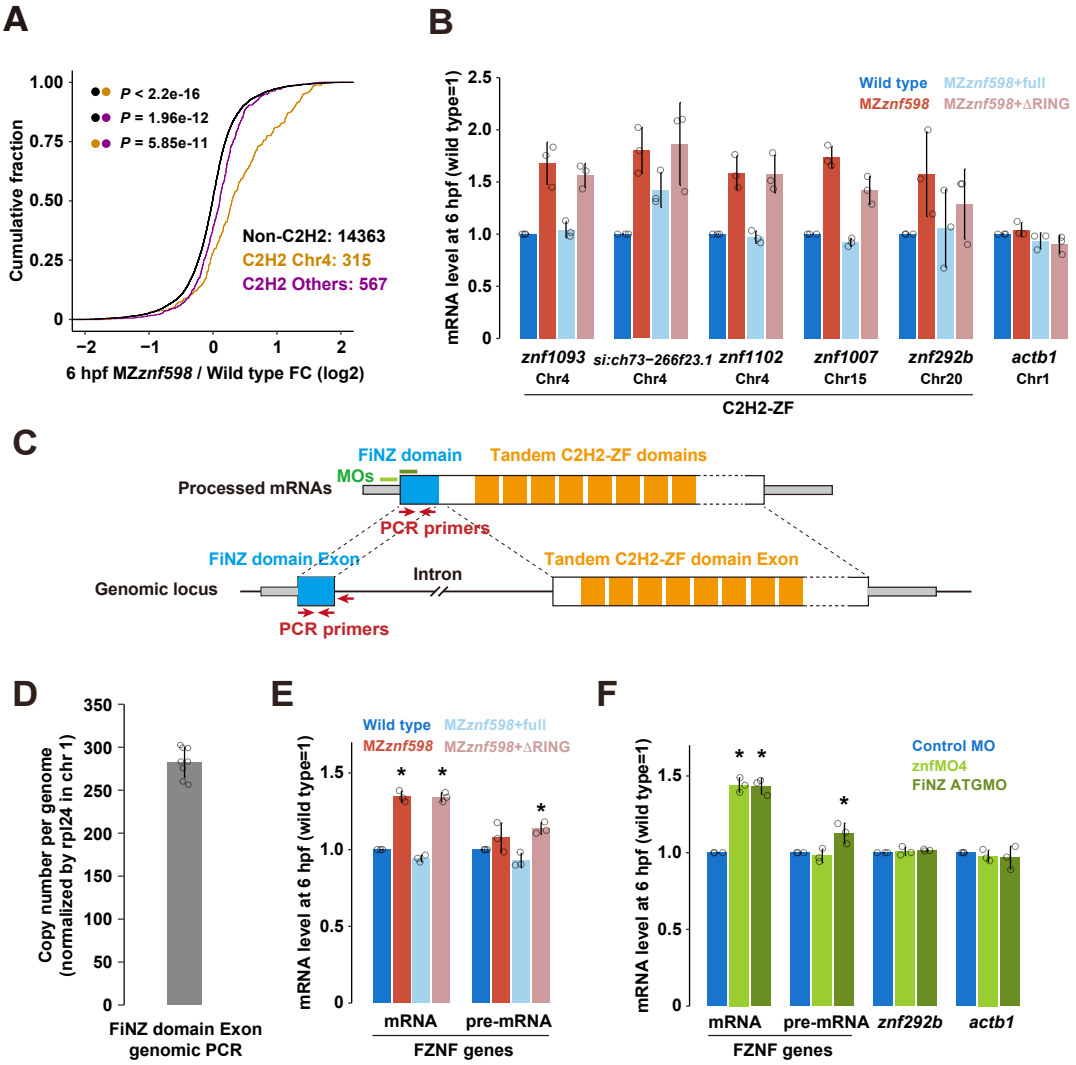

Ishibashi *et al.* Figure 5

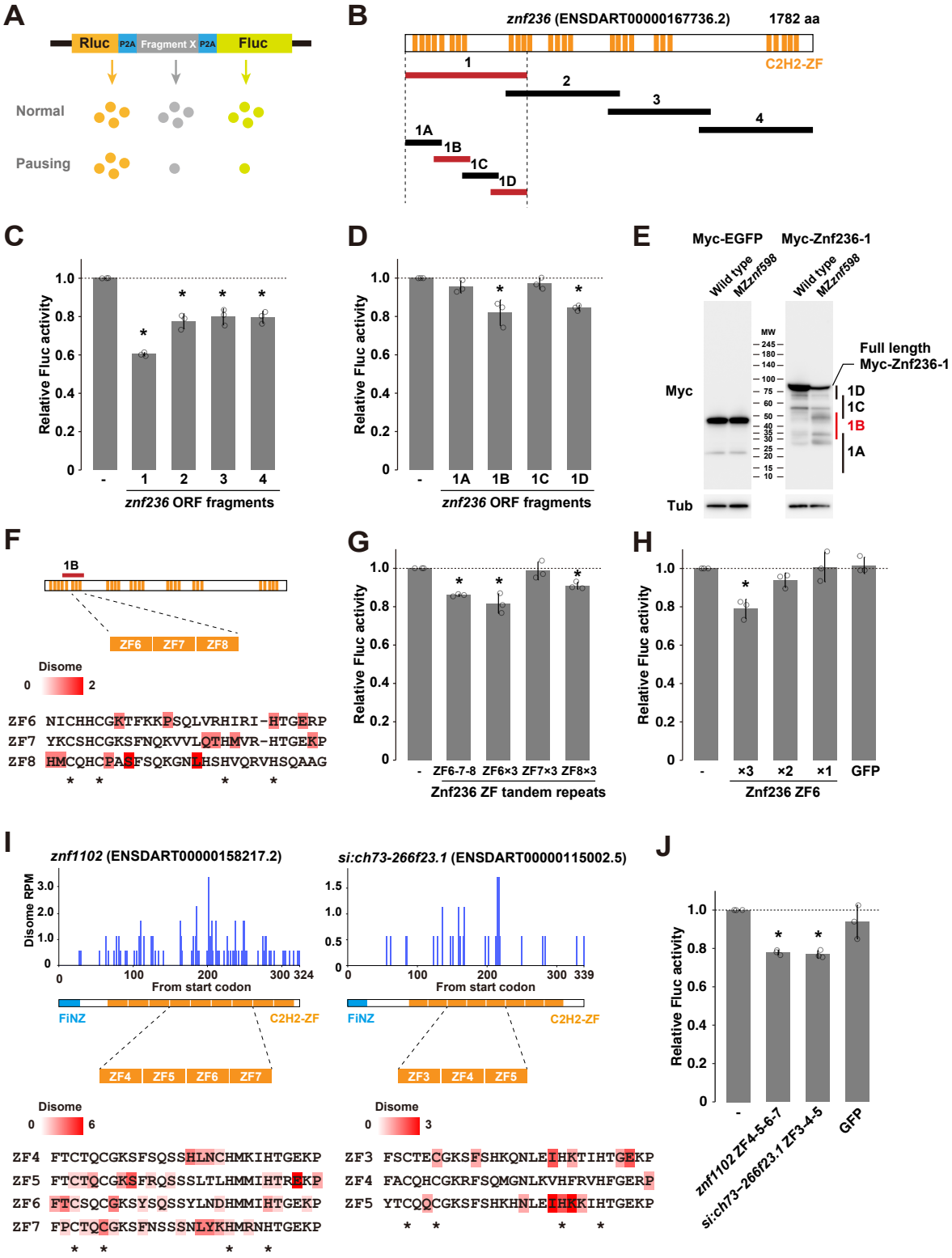

Ishibashi *et al.* Figure 6

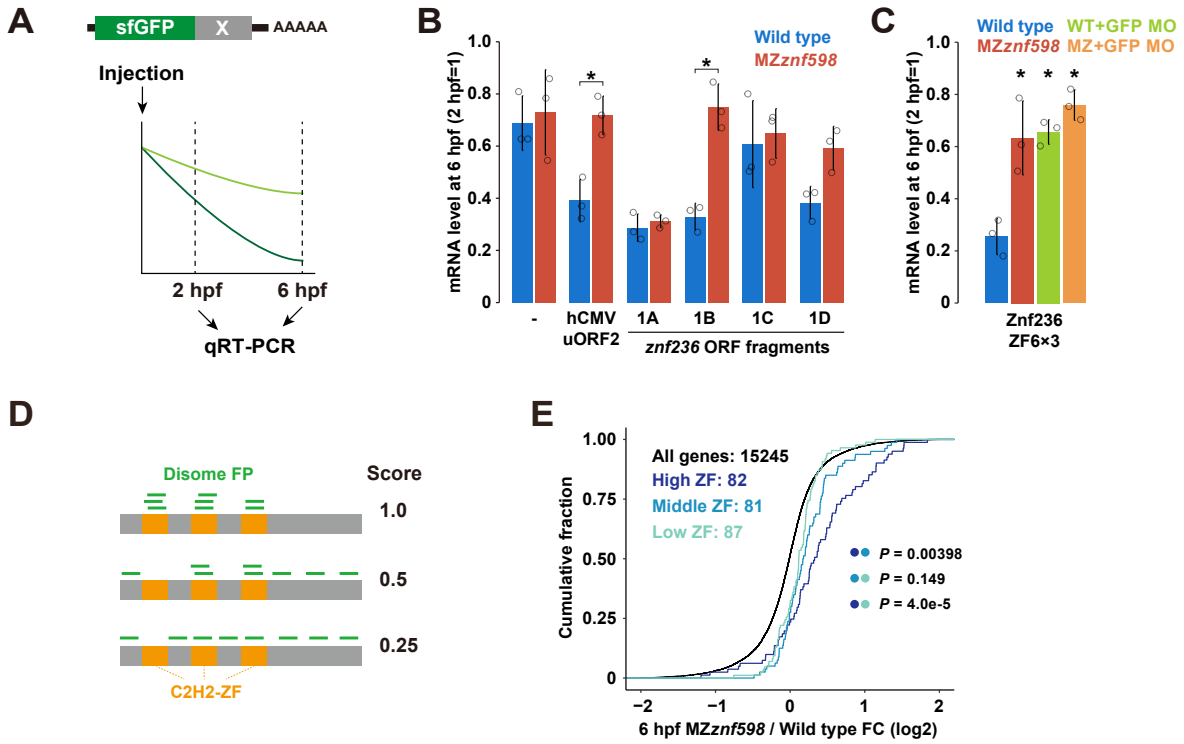

Ishibashi *et al.* Figure 7

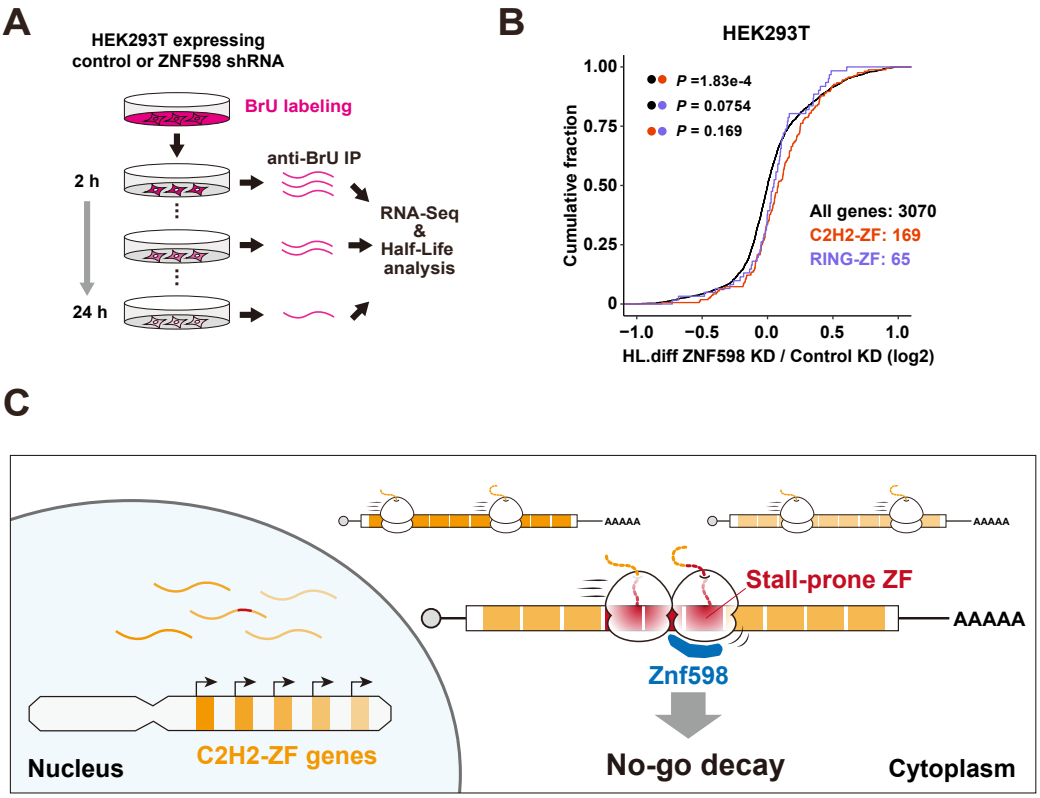

Ishibashi et al., Supplemental Figure 1

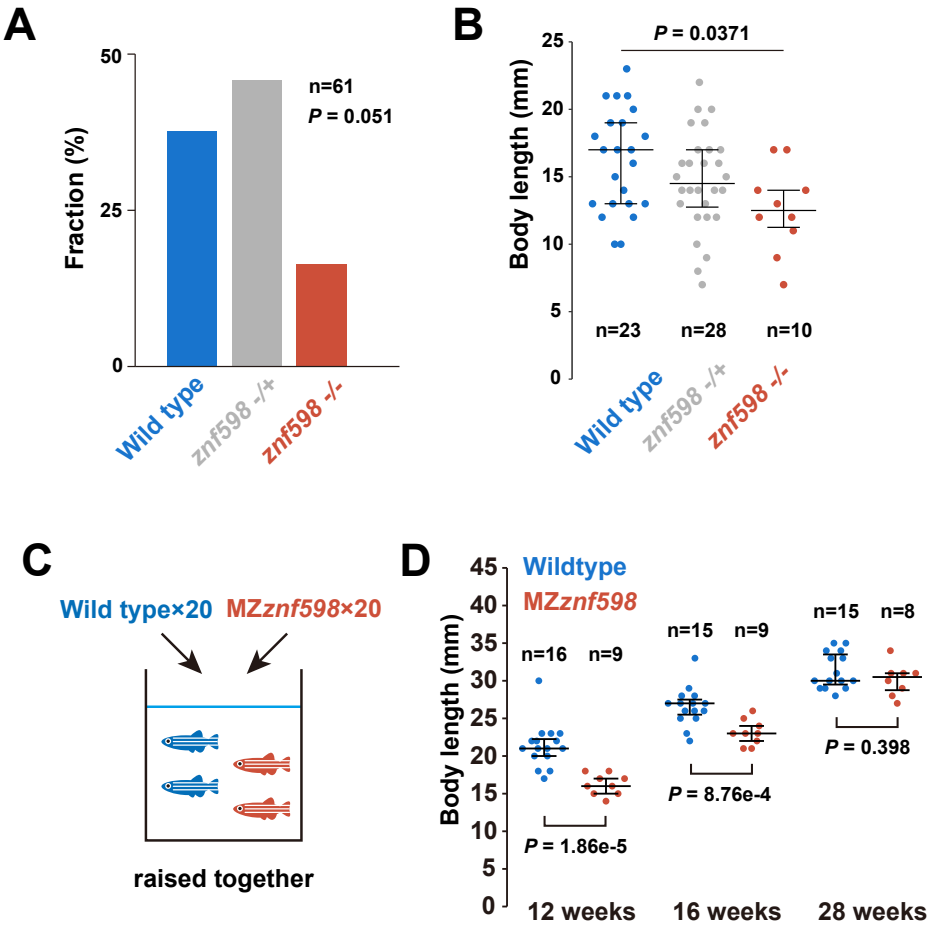

Ishibashi *et al*., Supplemental Figure 2

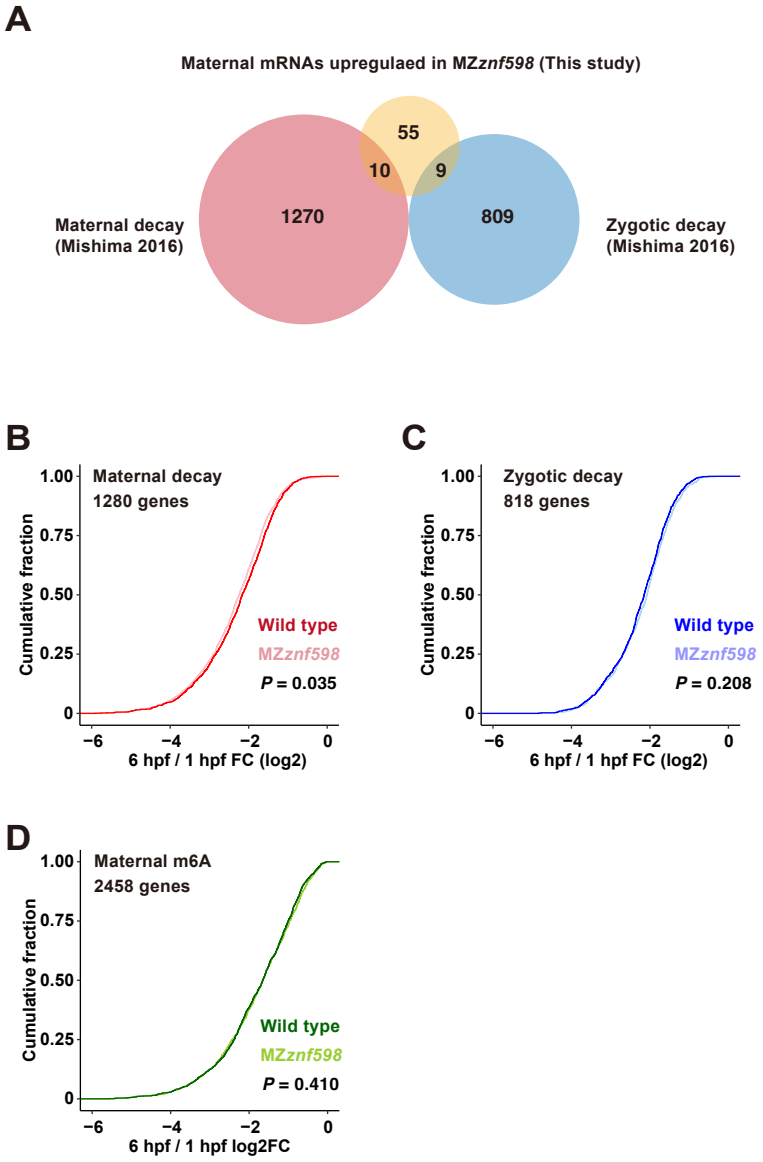

Ishibashi *et al*., Supplemental Figure 3

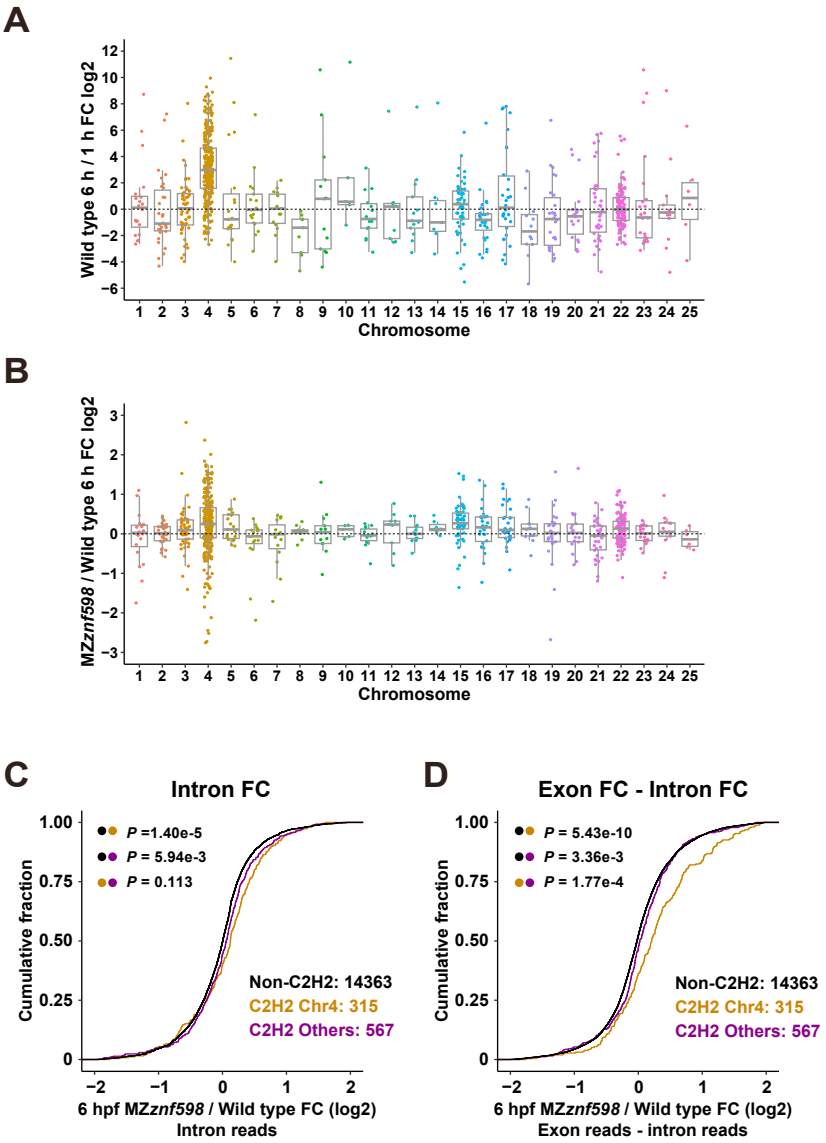

Ishibashi *et al.*, Supplemental Figure 4

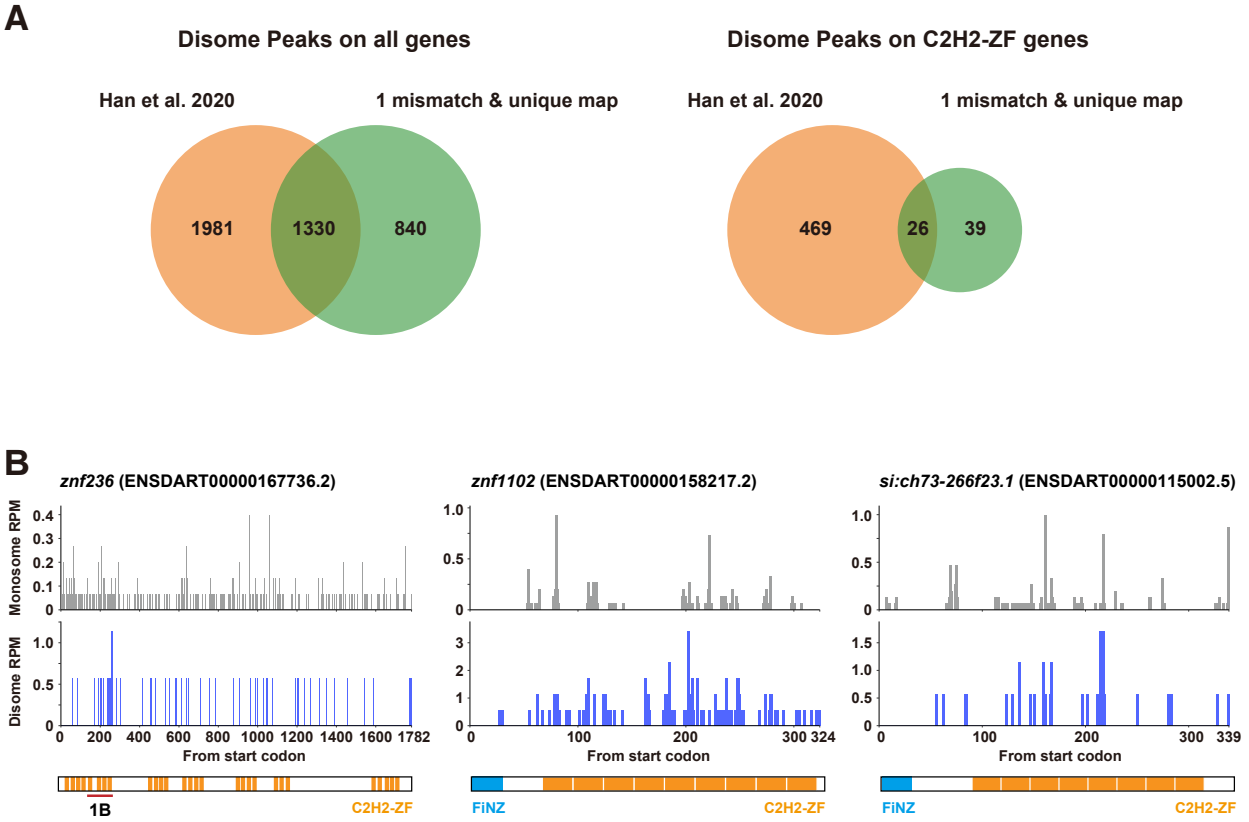

Ishibashi *et al.*, Supplemental Figure 5

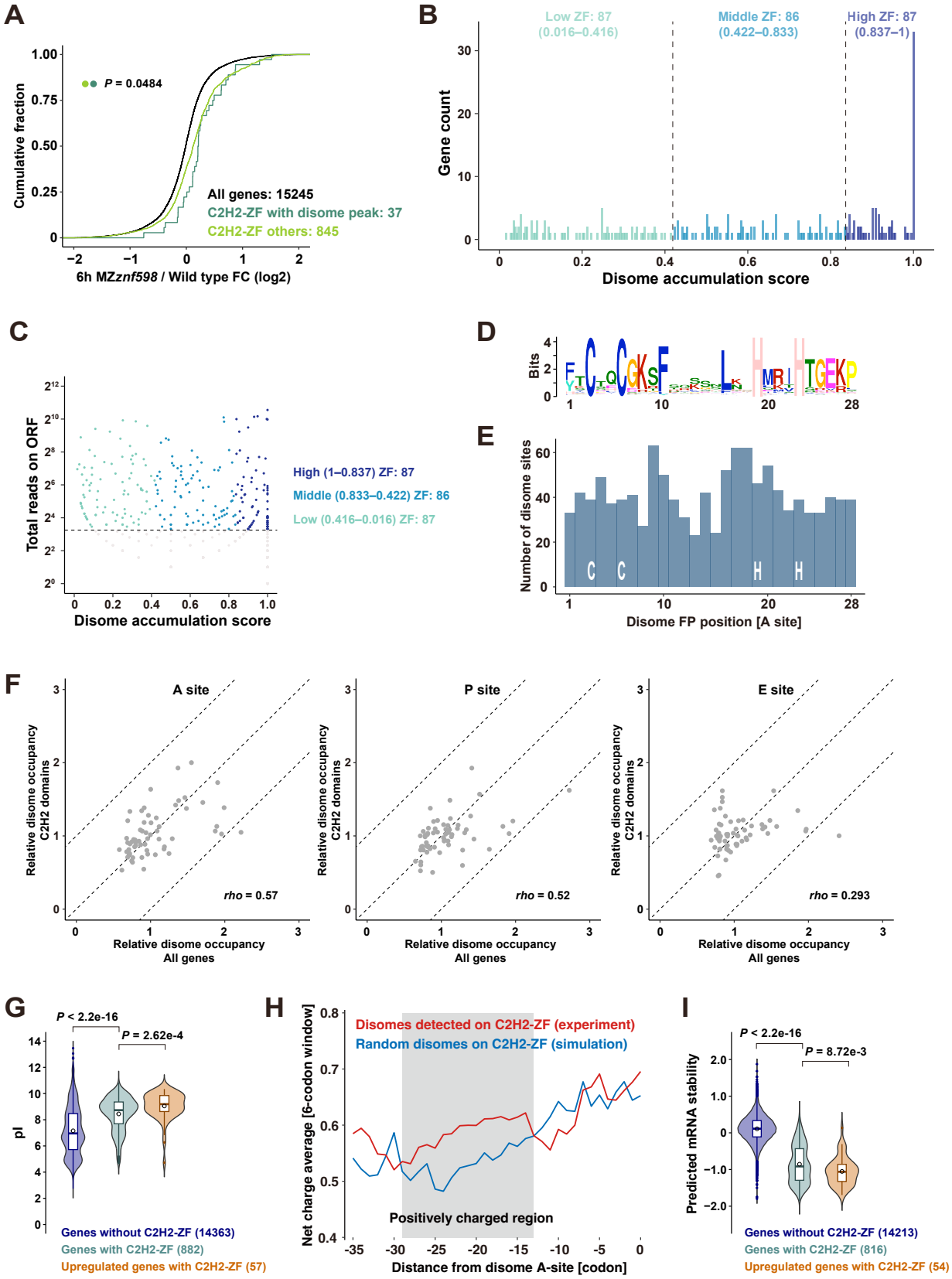
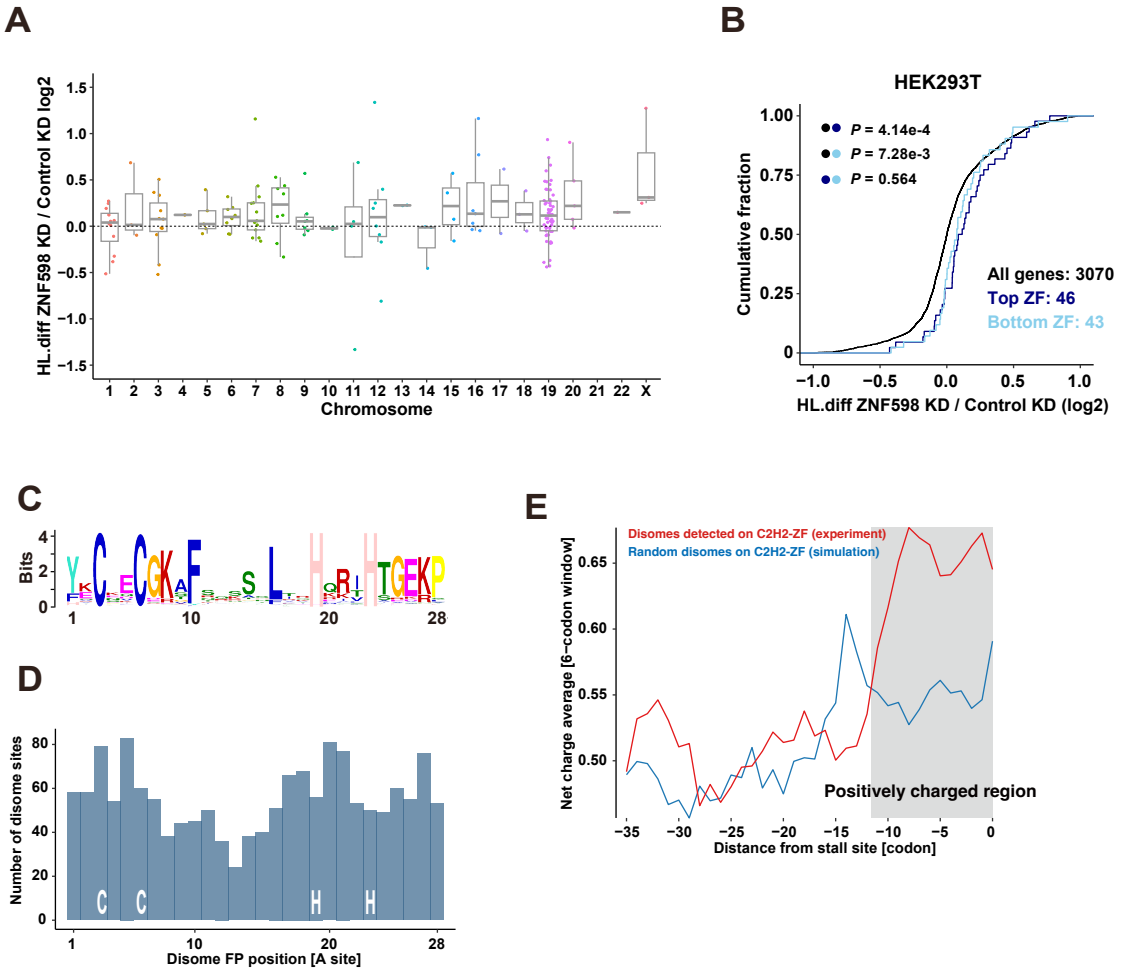
Ishibashi *et al*., Supplemental Figure 6